JAXA Research and Development Report

The Development of a New Viscous Shock-Layer Code for Computing Hypersonic Flows around Blunted Body and Its Applications

Shigeru KUCHI-ISHI

October 2005

Japan Aerospace Exploration Agency

Contents

The Development of a New Viscous Shock-Layer Code for Computing Hypersonic Flows around Blunted Body and Its Applications

Shigeru Kuchi-Ishi[*]

鈍頭物体周り極超音速流計算用新規粘性衝撃層コードの開発およびその応用

口石　茂[*]

ABSTRACT

A numerical code has been developed to solve the Viscous Shock-Layer (VSL) equations for chemically reacting hypersonic flows around a blunted body. The code basically follows the original solution procedure found in other VSL codes, but some specific treatments have been considered and implemented to enhance the accuracy and robustness. In the present article, the governing equations and physical models employed are firstly presented and then the method of solution is described in detail. By using the present code, it has become possible to solve chemically nonequilibrium flows around a hemisphere typically within 1 minute using a conventional personal computer. The accuracy of the code is validated by comparing with the computational results of other VSL/Navier-Stokes codes and available experimental data. It is shown that the difference between Navier-Stokes results in the stagnation heat flux for perfect gas flow is around 1 % at most for a Reynolds number range from 10^3 to 10^5. Further, an approach to solving stagnation streamline profiles both quickly and accurately under the framework of the present VSL algorithm is proposed and its accuracy and availability are examined. Also proposed is an algorithm which computes the free stream properties of ground-based high enthalpy test facilities from the measured stagnation point heat flux and Pitot pressure as an inverse problem of the VSL analysis. The stagnation point analysis method developed is implemented in this algorithm and the accuracy and reliability of this approach are examined.

Keywords: hypersonic flow, viscous shock-layer analysis, stagnation streamline, free stream properties

概　　　要

鈍頭物体周り極超音速化学反応流に関する粘性衝撃層 (VSL) 方程式の数値解析コードが開発された。本コードは基本的に過去に提案された VSL 解法に従っているが、精度および安定性向上の目的でいくつかの改良が試みられている。本論文では、基礎方程式および物理モデルについてまず記述され、次に解法の詳細が述べられる。本コードにより、半球周り化学的非平衡流を、パーソナルコンピューターを用いて 1 分以内で解くことが可能となった。本コードの妥当性は他の VSL/ナヴィエ・ストークスコードによる計算結果および試験データと比較することにより検証される。完全気体の場合ナヴィエ・ストークス解析の結果との差は、レイノルズ数 10^3–10^5 の範囲で高々 1 % 程度であることが示される。また本 VSL 解法を基礎とした、鈍頭物体周り流れの淀み流線のみを高速かつ高精度に解く手法が提案され、その精度および有効性が議論される。さらに高エンタルピ試験設備の気流条件を、測定された淀み点加熱率およびピトー圧の情報を用いて、VSL 解析の逆解法として求めるアルゴリズムが考案され、淀み流線解析手法と組み合わせることにより、実用上十分な計算時間で解を得ることが可能であることが示される。

Nomenclature

C_i = mass concentration of species i, ρ_i^*/ρ^*

$C_{p,i}$ = specific heat at constant pressure, $C_{p,i}^*/C_{p\infty}^*$

$C_{v\,\mathrm{vib},i}$ = specific heat of vibration, $C_{v\,\mathrm{vib},i}^*/C_{p\infty}^*$

D_i = effective diffusion coefficient, $D_i^*/\mu_{\mathrm{ref}}^*$

$E_{\mathrm{D},i}$ = dissociation energy per unit mass, $E_{\mathrm{D},i}^*/U_\infty^{*\,2}$

$E_{\mathrm{I},r}$ = ionization energy per particle of electron-impact ionization r, $E_{\mathrm{I},r}^*/U_\infty^{*\,2}$

$e_{\mathrm{vib},i}$ = vibrational energy per unit mass, $e_{\mathrm{vib},i}^*/U_\infty^{*\,2}$

h_i = static enthalpy per unit mass, $h_i^*/U_\infty^{*\,2}$

Δh_i^0 = heat of formation of species i at absolute zero

J_i = diffusion mass flux in the direction normal to the body, $J_i^* R_{\mathrm{n}}^*/\mu_{\mathrm{ref}}^*$

k^* = Boltzmann constant

m_i^* = mass of species i

M_i^* = molecular weight of species i

$\overline{M}^*$ = mixture molecular weight, $(\sum_i C_i/M_i^*)^{-1}$

M_∞ = free stream Mach number

n_i = number density of species i

p = static pressure, $p^*/(\rho_\infty^* U_\infty^{*\,2})$

q = heat flux, $q^*/(\rho_\infty^* U_\infty^{*\,3})$

$\Re^*$ = universal gas constant

R_i^* = gas constant of species i, $\Re^*/M_i^*$

R_{n}^* = body nose radius

r = radius measured from axis of symmetry to a point on the body surface, r^*/R_{n}^*

s = coordinate measured along the body surface, s^*/R_{n}^*

T = temperature, T^*/T_{ref}^*

T_{ref}^* = reference temperature, $U_\infty^{*\,2}/C_{p\infty}^*$

U_∞^* = free stream velocity

u = velocity component tangent to the body surface, u^*/U_∞^*

v = velocity component normal to the body surface, v^*/U_∞^*

V_i^y = diffusion velocity component normal to the body surface, $V_i^{y*}\rho_\infty^* R_{\mathrm{n}}^*/\mu_{\mathrm{ref}}^*$

X_i = mole fraction of species i, $(\overline{M}^*/M_i^*)C_i$

y = coordinate measured normal to body surface, y^*/R_{n}^*

$\dot{w}_i$ = mass production rate of species i per unit volume, $\dot{w}_i^* R_{\mathrm{n}}^*/(\rho_\infty^* U_\infty^*)$

z = coordinate measured along body axis, z^*/R_{n}^*

α = angle between shock tangent and axis

ϵ = Reynolds number parameter, $\sqrt{\mu_{\mathrm{ref}}^*/\rho_\infty^* U_\infty^* R_{\mathrm{n}}^*}$

ε = surface emissivity

θ_r^* = characteristic temperature of reaction r

$\Theta_{\mathrm{vib},i}^*$ = characteristic temperature of vibration

κ = surface curvature, $\kappa^* R_{\mathrm{n}}^*$

λ = thermal conductivity, $\lambda^*/(\mu_{\mathrm{ref}}^* C_{p\infty}^*)$

μ = viscosity, $\mu^*/\mu_{\mathrm{ref}}^*$

μ_{ref}^* = viscosity evaluated at T_{ref}^*

ρ = density, ρ^*/ρ_∞^*

α = angle between body tangent and axis

σ^* = Stefan-Boltzmann constant

$\sigma_{i,j}^*$ = effective cross section for $i-j$ collision

ξ = coordinate measured along the body surface (same as s)

Subscripts

i = species index

w   = wall value

∞ = free stream value

r = reaction index

stg   = stagnation point value

Superscripts

$*$ = dimensional quantities

$'$ = differentiation with respect to ξ

1   Introduction

The motivation of the present work lies in finding a new possibility for the application of the Viscous Shock-Layer (VSL) method to today's hypersonic problems. The VSL algorithm was developed by Davis in 1970 [1], and was an alternative method of solving Navier-Stokes (NS) equations. This is because, at that time, it was essentially impossible to solve Navier-Stokes equations directly due to the limitation of computer performance. Needless to say, the rapid progress of computational resources makes it much easier to solve the Navier-Stokes equations even for three-dimensional complex flow fields. However, even today, the VSL algorithm is expected to be useful for practical design process of a reentry vehicle design or other purposes. Compared to conventional Navier-Stokes solvers, the VSL method has several favorable properties including:

1. The VSL equations can be solved by a space-marching procedure, which is very efficient in terms of computing time and storage requirements.

2. Every equation is written in nonconservative form and, after the discretization, is reduced to tridiagonal simultaneous linear algebraic equations in terms of primitive variables at each shock-layer location. This system of equations can readily be solved and convergence speed is expected to be much faster than NS solvers which discretize the equations for conservative variables and obtain a steady-state solution as an asymptotic solution of time-marching algorithm.

3. The equation system is formulated in body-oriented coordinates, which is mathematically rigorous. Then the method is free from a series of errors regarding the numerical evaluation of the metrics. This kind of error is inevitable for NS solvers as long as the flow field is solved using the generalized coordinate system.

4. The VSL method is a shock-fitting scheme and only the flow inside the shock-layer is computed. Then there is no need to add additional numerical dissipation terms which degrade the spacial accuracy but are inevitably required to capture shock waves stably for NS solvers.

5. The equations are solved successively contrary to the shock-capturing scheme which solves the equations in a coupled way. This has an advantage that it is easy to reduce or add an additional equation in accordance with a change of physical models. Also, as the number of equations increases, the total amount of computational time increases only linearly.

6. Since the VSL method is a space-marching scheme, the solution procedure starts from solving flow field properties along the stagnation streamline. On the other hand, if we can specify the appropriate downstream information in advance, it is possible to solve the flow field only along the stagnation streamline.

The last item is of particulary interest. For quite many problems, we are only interested in information concerning the stagnation property of blunt body flows. In this case, it is much better from the viewpoint of computational efficiency if we can find a way to solve only the stagnation region, not solving the whole flow field.

On the other hand, it should be kept in mind that the VSL equations are an approximation of the NS equations. Then it is very important to investigate the range of applicability of this system of equations. The VSL equations are obtained from the steady-state NS equations by keeping terms up to second order in the inverse square root of the Reynolds number. The accuracy of the VSL equations, therefore, degrades as the Reynolds number decreases. In the present study, the accuracy of the VSL solution is investigated by comparing the NS solutions for a wide range of Reynolds and Mach numbers.

Although the VSL method has nice properties as mentioned above, there are several limitations to this method. Since the VSL method is a space marching scheme, it cannot be applied for a flow field which includes separation. Thus the application of the VSL method to a complex geometry is basically impossible. Even for a relatively simple body configuration, we sometimes encounter difficulties in solving the equations stably. For example, if we try to solve the flow field around a sphere-cone configuration, the surface curvature becomes discontinuous at the sphere-cone tangent point. Since the body-curvature terms explicitly appear in the VSL equations, this discontinuity makes the computation very unstable and sometimes we fail to obtain converged solutions. Thus the application of the VSL method is inevitably limited to a relatively simple flow field. However, if we consider simple problems such as the flow field around hemisphere, the VSL method still gives us a lot of possibilities to apply to problems which are enormously expensive or essentially impossible to solve if a NS code is employed as flow field solver.

In the present work, a new numerical code has been developed which solves VSL equations for chemically reacting flows around a blunted body at hypersonic speeds. The overall method of solution employed in the present code is basically similar to the one employed in the original solution procedure of Davis [1] and other subsequent publications (Refs. [2]–[4]). However, the method developed here differs in certain basic respects as follows:

1. To solve VSL equations, an initial shock shape is required as input for the solution method to march in the streamwise direction. In the preceding VSL codes, this is obtained by various procedures, each requiring considerable computational effort. In the present code, this is given by a very simple analytical formula based on experimental data and then the additional computational requirement is negligible.

2. Conventionally, the continuity equation and normal momentum equation are coupled to overcome the convergence problems. In the present code, on the contrary, these equations are solved sequentially with other equations. Thus the algorithm is much simpler and more computationally efficient without losing robustness and accuracy of the code.

3. Most VSL solvers discretize the equation system for streamwise first derivatives using two-point backward difference. On the contrary, in the present code, the streamwise gradients are evaluated using second-order three-point backward difference. However, difficulties exist when solving the normal momentum equation using the three-point backward difference. Some special treatments to solve this equation has been therefore considered and implemented.

In the present article, basic assumptions, governing equations and descriptions of various physical models are firstly presented. Then the method of discretization of the equation system is discussed in detail. The accuracy of the code developed is validated by comparing the computational results with other VSL and Navier-Stokes codes, available experimental data, and a correlation formula which has been proposed. An approach which makes it possible to obtain stagnation properties by solving only the stagnation streamline is also developed. This technique is further applied to a new method to obtain free stream properties of hypersonic/high-enthalpy test facilities with using measured stagnation point heat flux and Pitot pressure.

2   Numerical analysis

2.1   Governing equations

The governing equations are axi-symmetric viscous shock-layer equations formulated for a multi-component gas with thermochemical nonequilibrium (Refs. [3] and [5]). In the formulation, the following assumptions are introduced:

1. The shock-layer gas is composed of a maximum of 11 species (N_2, O_2, NO, N, O, N_2^+, O_2^+, NO^+, N^+, O^+ and e^-). As the charge neutrality of the gas mixture is also assumed, the density of electron is given by

$$\rho_e = \sum_{i=I} \frac{M_e}{M_i} \rho_i \tag{2.1}$$

   where $\sum_{i=I}$ indicates the summation over all ionic species. Hence, only 10 species except for electrons are independent for this chemical system.

2. A harmonic oscillator model is employed to describe molecular vibration. Vibrational energy levels of a molecular species are populated according to a Boltzmann distribution corresponding to a vibrational temperature.

3. Rotational, vibrational, and electron temperature of molecules are in equilibrium with the translational temperature of heavy particles. All the translational temperatures of heavy particles are equal.

4. The effect of the electronic excitation energy on the flow is negligible compared with that of other energy modes.

5. The gas in the shock-layer does not emit or absorb radiation.

The VSL equations are derived from the steady-state Navier-Stokes equations written for a body-intrinsic coordinate system (s, y) as shown in Fig. 2.1. The equations are first nondimensionalized by reference variables as shown in the Nomenclature. A set of equations is then obtained by keeping terms up to second order in a Reynolds number parameter, $\epsilon = 1/\sqrt{Re}$. The present VSL equations are composed of continuity, momentum, energy, and species conservation equations. They are written in the following non-dimensional form:

Continuity equation:

$$\frac{\partial}{\partial s}\left[(r + y\cos\phi)\rho u\right] + \frac{\partial}{\partial y}\left[(1 + \kappa y)(r + y\cos\phi)\rho v\right] = 0 \tag{2.2}$$

s-momentum equation:

$$\frac{\rho u}{1 + \kappa y}\frac{\partial u}{\partial s} + \rho v\frac{\partial u}{\partial y} + \frac{\kappa\rho uv}{1 + \kappa y} + \frac{1}{1 + \kappa y}\frac{\partial p}{\partial s} = \epsilon^2\frac{\partial}{\partial y}\left[\mu\left(\frac{\partial u}{\partial y} - \frac{\kappa u}{1 + \kappa y}\right)\right]$$
$$+ \epsilon^2\mu\left(\frac{2\kappa}{1 + \kappa y} + \frac{\cos\phi}{r + y\cos\phi}\right)\left(\frac{\partial u}{\partial y} - \frac{\kappa u}{1 + \kappa y}\right) \tag{2.3}$$

y-momentum equation:

$$\frac{\partial p}{\partial y} = \frac{\kappa}{1 + \kappa y}\rho u^2 - \frac{1}{1 + \kappa y}\rho u\frac{\partial v}{\partial s} - \rho v\frac{\partial v}{\partial y} \tag{2.4}$$

Energy equation:

$$\frac{\rho u}{1 + \kappa y}C_p\frac{\partial T}{\partial s} + \rho v C_p\frac{\partial T}{\partial y} - \frac{u}{1 + \kappa y}\frac{\partial p}{\partial s} - v\frac{\partial p}{\partial y} = \epsilon^2\frac{\partial}{\partial y}\left(\lambda\frac{\partial T}{\partial y}\right)$$
$$+ \epsilon^2\left(\frac{\kappa}{1 + \kappa y} + \frac{\cos\phi}{r + y\cos\phi}\right)\left(\lambda\frac{\partial T}{\partial y}\right) - \epsilon^2\sum_i J_i C_{p,i}\frac{\partial T}{\partial y}$$
$$+ \epsilon^2\mu\left(\frac{\partial u}{\partial y} - \frac{\kappa u}{1 + \kappa y}\right)^2 - \sum_i h_i\dot{w}_i \tag{2.5}$$
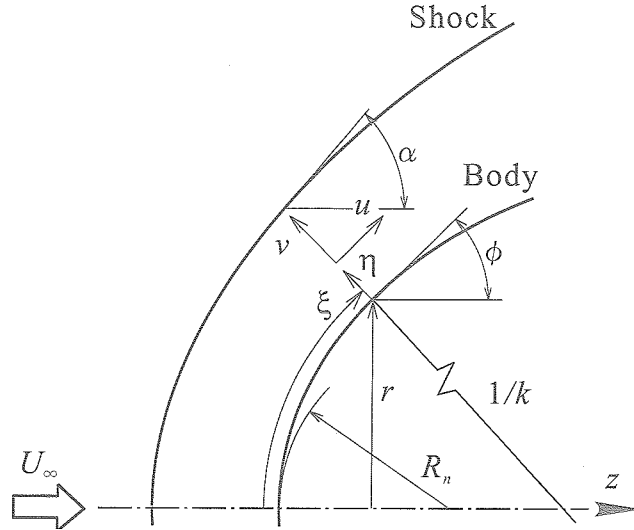
Figure 2.1: Coordinate system

Species conservation equation:

$$\frac{\rho u}{1 + \kappa y} \frac{\partial C_i}{\partial s} + \rho v \frac{\partial C_i}{\partial y} = \dot{w}_i - \epsilon^2 \frac{\partial J_i}{\partial y} - \epsilon^2 \left(\frac{\kappa}{1 + \kappa y} + \frac{\cos \phi}{r + y \cos \phi} \right) J_i \qquad (2.6)$$

Equation of state:

$$p = \frac{\rho \mathfrak{R}^*}{C_{p,\infty}^*} \sum_i \frac{C_i}{M_i^*} T \qquad (2.7)$$

Further if non-reacting gas is assumed, the last term of Eq. (2.5), which represents the energy production rate due to chemical reaction, is omitted.

2.2 Transformation of the governing equations

The independent and dependent variables (except for the species mass concentration and transport properties) are normalized by the values behind the shock at each shock-layers. When the normal coordinate y is normalized by the local shock-layer thickness, y_{sh}, a constant number of finite-difference grid points between the body and the shock can be used even if local shock-layer thickness is updated in the solution procedure. The normalization is made as follows:

$$\begin{aligned} \xi = s, \qquad \eta = y/y_{\mathrm{sh}}, \quad \overline{u} = u/u_{\mathrm{sh}}, \quad \overline{v} = v/v_{\mathrm{sh}}, \\ \overline{p} = p/p_{\mathrm{sh}}, \quad \overline{\rho} = \rho/\rho_{\mathrm{sh}}, \quad \overline{T} = T/T_{\mathrm{sh}} \end{aligned} \qquad (2.8)$$

The transformations relating the differential expressions are

$$\frac{\partial}{\partial s} = \frac{\partial}{\partial \xi} - \eta \frac{y_{\mathrm{sh}}'}{y_{\mathrm{sh}}} \frac{\partial}{\partial \eta} \qquad (2.9)$$

$$\frac{\partial}{\partial y} = \frac{1}{y_{\mathrm{sh}}} \frac{\partial}{\partial \eta} \qquad (2.10)$$

$$\frac{\partial^2}{\partial y^2} = \frac{1}{y_{\mathrm{sh}}^2} \frac{\partial^2}{\partial \eta^2} \qquad (2.11)$$

where

$$y_{\mathrm{sh}}' = \frac{dy_{\mathrm{sh}}}{d\xi} \qquad (2.12)$$

When the VSL equations are written in the transformed coordinate system (ξ, η), the s-momentum, energy, and species conservation equations can be expressed in the following standard form for a parabolic

partial differential equation:

$$\frac{\partial^2 W}{\partial \eta^2} + A_1 \frac{\partial W}{\partial \eta} + A_2 W + A_3 + A_4 \frac{\partial W}{\partial \xi} = 0 \tag{2.13}$$

where W represents $\overline{u}$ in the s-momentum equation, $\overline{T}$ in the energy equation, and C_i in the species mass conservation equations. The coefficients A_1 through A_4 are functions of the independent and dependent variables and may be written as follows:

s-momentum equation: $W = \overline{u}$

$$A_1 = \frac{1}{\mu}\frac{\partial \mu}{\partial \eta} + \frac{\kappa y_{\text{sh}}}{1 + \kappa y_{\text{sh}}\eta} + \frac{y_{\text{sh}}\cos\phi}{r + y_{\text{sh}}\eta\cos\phi} + \frac{y_{\text{sh}}y_{\text{sh}}'\rho_{\text{sh}}u_{\text{sh}}\overline{\rho u}\eta}{\epsilon^2\mu(1+\kappa y_{\text{sh}}\eta)}$$
$$- \frac{y_{\text{sh}}\rho_{\text{sh}}v_{\text{sh}}\overline{\rho v}}{\epsilon^2\mu} \tag{2.14}$$

$$A_2 = -\frac{\kappa y_{\text{sh}}}{1 + \kappa y_{\text{sh}}\eta}\frac{1}{\mu}\frac{\partial \mu}{\partial \eta} - \frac{\kappa^2 y_{\text{sh}}^2}{(1+\kappa y_{\text{sh}}\eta)^2} - \frac{\kappa y_{\text{sh}}^2\cos\phi}{(1+\kappa y_{\text{sh}}\eta)(r+y_{\text{sh}}\eta\cos\phi)}$$
$$- \frac{y_{\text{sh}}^2\rho_{\text{sh}}u_{\text{sh}}'\overline{\rho u}}{\epsilon^2(1+\kappa y_{\text{sh}}\eta)\mu} - \frac{\kappa y_{\text{sh}}^2\rho_{\text{sh}}v_{\text{sh}}\overline{\rho v}}{\epsilon^2(1+\kappa y_{\text{sh}}\eta)\mu} \tag{2.15}$$

$$A_3 = -\frac{y_{\text{sh}}^2}{\epsilon^2 u_{\text{sh}}(1+\kappa y_{\text{sh}}\eta)\mu}\left[\overline{p}p_{\text{sh}}' + p_{\text{sh}}\frac{\partial \overline{p}}{\partial \xi} - \eta\frac{y_{\text{sh}}'}{y_{\text{sh}}}p_{\text{sh}}\frac{\partial \overline{p}}{\partial \eta}\right] \tag{2.16}$$

$$A_4 = -\frac{y_{\text{sh}}^2\rho_{\text{sh}}u_{\text{sh}}\overline{\rho u}}{\epsilon^2(1+\kappa y_{\text{sh}}\eta)\mu} \tag{2.17}$$

Energy equation: $W = \overline{T}$

$$A_1 = \frac{1}{\lambda}\frac{\partial \lambda}{\partial \eta} + \frac{\kappa y_{\text{sh}}}{1 + \kappa y_{\text{sh}}\eta} + \frac{y_{\text{sh}}\cos\phi}{r + y_{\text{sh}}\eta\cos\phi} - \frac{y_{\text{sh}}}{\lambda}\sum_i J_i C_{p,i}$$
$$- \frac{y_{\text{sh}}\rho_{\text{sh}}C_p\overline{\rho}}{\epsilon^2\lambda}\left[v_{\text{sh}}\overline{v} - \frac{u_{\text{sh}}y_{\text{sh}}'\overline{u}\eta}{1+\kappa y_{\text{sh}}\eta}\right] \tag{2.18}$$

$$A_2 = A_4\frac{1}{T_{\text{sh}}}T_{\text{sh}}' - \frac{y_{\text{sh}}^2\dot{w}_2}{\epsilon^2\lambda} \tag{2.19}$$

$$A_3 = -\frac{y_{\text{sh}}^2\dot{w}_1}{\epsilon^2 T_{\text{sh}}\lambda} + \frac{y_{\text{sh}}^2\mu}{T_{\text{sh}}\lambda}\left[\frac{u_{\text{sh}}}{y_{\text{sh}}}\frac{\partial \overline{u}}{\partial \eta} - \frac{\kappa u_{\text{sh}}\overline{u}}{1+\kappa y_{\text{sh}}\eta}\right]^2 + \frac{y_{\text{sh}}p_{\text{sh}}v_{\text{sh}}\overline{v}}{\epsilon^2 T_{\text{sh}}\lambda}\frac{\partial \overline{p}}{\partial \eta}$$
$$+ \frac{y_{\text{sh}}^2 u_{\text{sh}}\overline{u}}{\epsilon^2(1+\kappa y_{\text{sh}}\eta)T_{\text{sh}}\lambda}\left[\overline{p}p_{\text{sh}}' + p_{\text{sh}}\frac{\partial \overline{p}}{\partial \xi} - \eta\frac{y_{\text{sh}}'}{y_{\text{sh}}}p_{\text{sh}}\frac{\partial \overline{p}}{\partial \eta}\right] \tag{2.20}$$

$$A_4 = -\frac{y_{\text{sh}}^2 C_p\rho_{\text{sh}}u_{\text{sh}}\overline{\rho u}}{\epsilon^2(1+\kappa y_{\text{sh}}\eta)\lambda} \tag{2.21}$$

Species conservation equation: $W = C_i$

$$A_1 = \frac{2}{\overline{M}^*}\frac{\partial \overline{M}^*}{\partial \eta} + \frac{1}{D_i}\frac{\partial D_i}{\partial \eta} + \frac{\kappa y_{\text{sh}}}{1 + \kappa y_{\text{sh}}\eta} + \frac{y_{\text{sh}}\cos\phi}{r + y_{\text{sh}}\eta\cos\phi}$$
$$+ \frac{y_{\text{sh}}y_{\text{sh}}'M_i^*\rho_{\text{sh}}u_{\text{sh}}\overline{\rho u}\eta}{\epsilon^2 D_i\overline{M}^*(1+\kappa y_{\text{sh}}\eta)} - \frac{y_{\text{sh}}M_i^*\rho_{\text{sh}}v_{\text{sh}}\overline{\rho v}}{\epsilon^2 D_i\overline{M}^*} \tag{2.22}$$

$$A_2 = \frac{1}{D_i\overline{M}^*}\frac{\partial D_i}{\partial \eta}\frac{\partial \overline{M}^*}{\partial \eta} + \frac{1}{\overline{M}^*}\frac{\partial^2 \overline{M}^*}{\partial \eta^2}$$
$$+ \frac{1}{\overline{M}^*}\frac{\partial \overline{M}^*}{\partial \eta}\left(\frac{\kappa y_{\text{sh}}}{1+\kappa y_{\text{sh}}\eta} + \frac{y_{\text{sh}}\cos\phi}{r + y_{\text{sh}}\eta\cos\phi}\right) - \frac{y_{\text{sh}}^2 M_i^*\rho_{\text{sh}}\overline{\rho}}{\epsilon^2 D_i\overline{M}^*}\dot{w}_i^1 \tag{2.23}$$

$$A_3 = \frac{y_{\text{sh}}^2 M_i^*\rho_{\text{sh}}\overline{\rho}}{\epsilon^2 D_i\overline{M}^*}\dot{w}_i^0 \tag{2.24}$$

$$A_4 = -\frac{y_{\text{sh}}^2 M_i^*\rho_{\text{sh}}u_{\text{sh}}\overline{\rho u}}{\epsilon^2 D_i\overline{M}^*(1+\kappa y_{\text{sh}}\eta)} \tag{2.25}$$

where $\overline{M}^* = (\sum_i C_i/M_i^*)^{-1}$. Also, $\dot{w}_i^0$, $\dot{w}_i^1$, $\dot{w}_1$, and $\dot{w}_2$ are coefficients represented by the following expressions:

$$\dot{w}_i/\rho = \dot{w}_i^0 - C_i\dot{w}_i^1 \tag{2.26}$$

$$\sum_i h_i\dot{w}_i = \dot{w}_1 + T_{\mathrm{sh}}\overline{T}\dot{w}_2 \tag{2.27}$$

The above two terms are treated implicitly to alleviate numerical instability coming from the strong nonlinearity of chemical reactions. The derivation of $\dot{w}_i^0$, $\dot{w}_i^1$, $\dot{w}_1$, and $\dot{w}_2$ is discussed in Section 4.4. The remaining equations are also rewritten as

Continuity equation:

$$\frac{\partial}{\partial\xi}[y_{\mathrm{sh}}(r + y_{\mathrm{sh}}\eta\cos\phi)\rho_{\mathrm{sh}}u_{\mathrm{sh}}\overline{\rho u}]$$
$$= \frac{\partial}{\partial\eta}[(r + y_{\mathrm{sh}}\eta\cos\phi)\{y_{\mathrm{sh}}'\rho_{\mathrm{sh}}u_{\mathrm{sh}}\overline{\rho u}\eta - (1 + \kappa y_{\mathrm{sh}}\eta)\rho_{\mathrm{sh}}v_{\mathrm{sh}}\overline{\rho v}\}] \tag{2.28}$$

y-momentum equation:

$$\frac{p_{\mathrm{sh}}}{y_{\mathrm{sh}}\rho_{\mathrm{sh}}u_{\mathrm{sh}}v_{\mathrm{sh}}}\frac{\partial\overline{p}}{\partial\eta} - \frac{\kappa u_{\mathrm{sh}}}{v_{\mathrm{sh}}(1 + \kappa y_{\mathrm{sh}}\eta)}\overline{\rho u}^2 + \frac{v_{\mathrm{sh}}\overline{\rho v}}{y_{\mathrm{sh}}u_{\mathrm{sh}}}\frac{\partial\overline{v}}{\partial\eta}$$
$$+ \frac{\overline{\rho u}}{1 + \kappa y_{\mathrm{sh}}\eta}\left(\frac{\partial\overline{v}}{\partial\xi} + \frac{\overline{v}}{v_{\mathrm{sh}}}v_{\mathrm{sh}}' - \frac{y_{\mathrm{sh}}'\eta}{y_{\mathrm{sh}}}\frac{\partial\overline{v}}{\partial\eta}\right) = 0 \tag{2.29}$$

Equation of state:

$$p_{\mathrm{sh}}\overline{p} = \frac{\rho_{\mathrm{sh}}\overline{\rho}\Re^*}{C_{p,\infty}^*}\sum_i\frac{C_i}{M_i^*}T_{\mathrm{sh}}\overline{T} \tag{2.30}$$

2.3 Boundary conditions

At the wall, no slip wall conditions for the velocity components and no temperature jump condition for the temperature are imposed:

$$u = 0 \tag{2.31}$$

$$v = 0 \tag{2.32}$$

$$T = T_{\mathrm{w}} \tag{2.33}$$

Zero normal gradient of the pressure is imposed on the wall:

$$\left(\frac{\partial p}{\partial y}\right)_{\mathrm{w}} = 0 \tag{2.34}$$

The wall temperature, T_{w}, is fixed to a specific value or determined by the radiative equilibrium condition:

$$q_{\mathrm{w}}^* + \widetilde{\varepsilon}\sigma^*T_{\mathrm{w}}^{*4} = 0 \tag{2.35}$$

where

$$q_{\mathrm{w}}^* = -\left[\lambda\frac{\partial T}{\partial y} - \sum_i h_i J_i\right]_{\mathrm{w}}^* \tag{2.36}$$

and $\widetilde{\varepsilon}$ is the emissivity of the wall surface.

The wall conditions of chemical species are governed by catalytic reactions on the wall and are obtained from the balance equations of the mass flux on the wall:

$$J_{i,\mathrm{w}}^* + k_{i,\mathrm{w}}^*\rho^*C_i = 0$$

where $k^*_{i,\mathrm{w}}$ is the coefficient of the loss rate of species i due to catalytic reaction on the wall, and $J^*_{i,\mathrm{w}}$ is diffusion mass flux in the direction normal to the wall. In the present analysis, three possible cases, namely non-catalytic wall (NCW), fully catalytic wall (FCW), and finite rate catalytic wall conditions are employed. For the NCW,

$$k^*_{i,\mathrm{w}} = 0$$

hence the species wall conditions become

$$J^*_{i,\mathrm{w}} = 0$$

Since the diffusion mass flux is proportional to the gradient of the species concentration according to Fick's law, the NCW condition is given by

$$\left(\frac{\partial C_i}{\partial y}\right)_{\mathrm{w}} = 0 \tag{2.37}$$

On the FCW, it is assumed that the chemical composition returns to the original composition, that is, the composition in the free stream:

$$C_{i,\mathrm{w}} = C_{i,\infty} \tag{2.38}$$

on the wall at an infinite rate. The FCW condition is corresponding to

$$k^*_{i,\mathrm{w}} \rightarrow \infty$$

for all the species except for N_2 and O_2.

For the finite rate catalytic wall, the catalytic recombination surface reaction rate constant $k^*_{i,\mathrm{w}}$ is expressed as

$$k^*_{i,\mathrm{w}} = \gamma_i \sqrt{\frac{\Re^* T^*_{\mathrm{w}}}{2\pi M^*_i}} \tag{2.39}$$

In the present study, according to Ref. [7], the energy transfer catalytic recombination coefficient for nitrogen atom γ_N is given as

$$\gamma_N = 0.0714 \exp(-2219/T^*_{\mathrm{w}}) \qquad 1090 < T^*_{\mathrm{w}} < 1670\,\mathrm{K} \tag{2.40}$$

whereas a constant value of 0.005 is specified for γ_O. The mass concentrations for other minor species including NO are set to be zero.

In the present analysis, it is assumed that no chemical reactions occur across the shock. Therefore, the boundary conditions immediately behind the shock are determined by solving the following frozen shock-jump relations:

$$\rho_{\mathrm{sh}}\widehat{v}_{\mathrm{sh}} = -\sin\alpha \tag{2.41}$$

$$\widehat{u}_{\mathrm{sh}} = \cos\alpha \tag{2.42}$$

$$p_{\mathrm{sh}} - \widehat{v}_{\mathrm{sh}}\sin\alpha = p^*_\infty/(\rho^*_\infty U^{*\,2}_\infty) + \sin^2\alpha \tag{2.43}$$

$$\sum_i C_{i,\mathrm{sh}}h_{i,\mathrm{sh}} + \frac{1}{2}\widehat{v}^2_{\mathrm{sh}} = \sum_i C_{i,\infty}h_{i,\infty} + \frac{1}{2}\sin^2\alpha \tag{2.44}$$

$$p_{\mathrm{sh}} = \rho_{\mathrm{sh}}\Re^* T_{\mathrm{sh}}/(\overline{M}^*_{\mathrm{sh}} C^*_{p\infty}) \tag{2.45}$$

where $\widehat{u}_{\mathrm{sh}}$ and $\widehat{v}_{\mathrm{sh}}$ are the velocity components tangent and normal to the shock, respectively. Then, the velocity components tangent and normal to the body denoted as u_{sh} and v_{sh} are expressed as

$$u_{\mathrm{sh}} = \widehat{u}_{\mathrm{sh}}\cos(\alpha - \phi) - \widehat{v}_{\mathrm{sh}}\sin(\alpha - \phi) \tag{2.46}$$

$$v_{\mathrm{sh}} = \widehat{u}_{\mathrm{sh}}\sin(\alpha - \phi) - \widehat{v}_{\mathrm{sh}}\cos(\alpha - \phi) \tag{2.47}$$

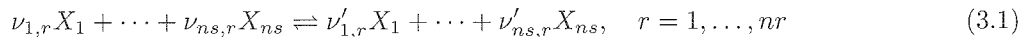The species mass concentrations behind the shock are set to be equal to their free stream values:

$$C_{i,\mathrm{sh}} = C_{i,\infty} \tag{2.48}$$

3 Gas model

In the present code, it is assumed that the free stream gas is air or nitrogen. In this section, all expressions are presented in terms of dimensional quantities and the superscript $*$ will not be used to denote dimensional quantities as done in the previous section.

3.1 Chemical reaction model

We consider nr elemental reactions in the chemical system involving ns species $(X_1, \ldots, X_{ns})$, of the general form,

$$\nu_{1,r}X_1 + \cdots + \nu_{ns,r}X_{ns} \rightleftharpoons \nu'_{1,r}X_1 + \cdots + \nu'_{ns,r}X_{ns}, \quad r = 1, \ldots, nr \tag{3.1}$$

Here, $\nu_{s,r}$ and $\nu'_{s,r}$ are the stoichiometric coefficients of the reactants and products of species s in the reaction r, respectively. The mass production rate of species i per unit volume due to chemical reaction, $\dot{w}_i$, can be written as

$$\frac{\dot{w}_i}{\rho} = M_i \sum_{r=1}^{nr} (\nu'_{i,r} - \nu_{i,r})(L_{\mathrm{f},r} - L_{\mathrm{b},r}) \tag{3.2}$$

where

$$L_{\mathrm{f},r} = k_{\mathrm{f},r}\rho^{\nu_r} \prod_{j=1}^{ns} \gamma_j^{\nu_{j,r}} \tag{3.3}$$

$$L_{\mathrm{b},r} = k_{\mathrm{b},r}\rho^{\nu'_r} \prod_{j=1}^{ns} \gamma_j^{\nu'_{j,r}} \tag{3.4}$$

$$\nu_r = \sum_{j=1}^{ns} \nu_{j,r} - 1 \tag{3.5}$$

$$\nu'_r = \sum_{j=1}^{ns} \nu'_{j,r} - 1 \tag{3.6}$$

$$\gamma_j = \frac{C_j}{M_j} \tag{3.7}$$

Twenty-four reactions shown in Table 3.1 are considered in this analysis for the 11-species air model. The reaction rates are given by the following expressions:

$$k_{\mathrm{f},r}(T) = C_r T^{s_r} \exp(-\theta_r/T), \quad (\mathrm{cm}^3/\mathrm{mol}) \tag{3.8}$$

$$k_{\mathrm{b},r}(T) = k_{\mathrm{f},r}(T)/K_r^{\mathrm{eq}}(T) \quad (\mathrm{cm}^3/\mathrm{mol} \text{ or } \mathrm{cm}^6/\mathrm{mol}^2) \tag{3.9}$$

The values of the constants C_r, s_r and θ_r are obtained from Refs. [9] and [10], and represented in Table 3.1.[†] Here, K_r^{eq} is the equilibrium constant, and the following approximate function is employed to evaluate K_r^{eq}:

$$K_r^{\mathrm{eq}}(T) = \exp\left[A_{1,r}/Z + A_{2,r} + A_{3,r}\ln Z + A_{4,r}Z + A_{5,r}Z^2\right]$$
(nondimensional value or $\mathrm{mol}/\mathrm{cm}^3$)
$$\tag{3.10}$$

$$Z = 10^4/T$$

The values of $A_{1,r}, \ldots, A_{5,r}$ are also obtained from Table 1.7 in Ref. [9].

[†]There is a typographical error in Ref. [9] for the nitrogen ionization rates ($r = 23$ in Table 3.1). The C value for nitrogen ionization should be 2.5×10^{34}, not 2.5×10^{33} as given in Ref. [9] (see Ref. [11]).

Table 3.1: Air chemistry and reaction rate constants

r	Reactants		Products	C_r	s_r	θ_r
1	$N_2 + M_1^a$	$\rightleftharpoons$	$N + N + M_1$	7.0×10^{21}	-1.6	$113,200$
2	$N_2 + M_2^b$	$\rightleftharpoons$	$N + N + M_2$	3.0×10^{22}	-1.6	$113,200$
3	$N_2 + e^-$	$\rightleftharpoons$	$N + N + e^-$	3.0×10^{24}	-1.6	$113,200$
4	$O_2 + M_1$	$\rightleftharpoons$	$O + O + M_1$	2.0×10^{21}	-1.5	$59,500$
5	$O_2 + M_2$	$\rightleftharpoons$	$O + O + M_2$	1.0×10^{22}	-1.5	$59,500$
6	$NO + M_3^c$	$\rightleftharpoons$	$N + O + M_3$	5.0×10^{15}	0.0	$75,500$
7	$NO + M_4^d$	$\rightleftharpoons$	$N + O + M_4$	1.1×10^{17}	0.0	$75,500$
8	$N_2 + O$	$\rightleftharpoons$	$NO + N$	6.4×10^{17}	-1.0	$38,400$
9	$NO + O$	$\rightleftharpoons$	$N + O_2$	8.4×10^{12}	0.0	$19,450$
10	$N + O$	$\rightleftharpoons$	$NO^+ + e^-$	8.8×10^8	1.0	$31,900$
11	$N + N$	$\rightleftharpoons$	$N_2^+ + e^-$	4.4×10^7	1.5	$67,500$
12	$O + O$	$\rightleftharpoons$	$O_2^+ + e^-$	7.1×10^2	2.7	$80,600$
13	$NO^+ + O$	$\rightleftharpoons$	$N^+ + O_2$	1.0×10^{12}	0.5	$77,200$
14	$O_2^+ + N$	$\rightleftharpoons$	$N^+ + O_2$	8.7×10^{13}	0.14	$28,600$
15	$NO + O^+$	$\rightleftharpoons$	$N^+ + O_2$	1.4×10^5	1.9	$15,300$
16	$O_2^+ + N_2$	$\rightleftharpoons$	$N_2^+ + O_2$	9.9×10^{12}	0.0	$40,700$
17	$O_2^+ + O$	$\rightleftharpoons$	$O^+ + O_2$	4.0×10^{12}	-0.09	$18,000$
18	$NO^+ + N$	$\rightleftharpoons$	$O^+ + N_2$	3.4×10^{13}	-1.08	$12,800$
19	$NO^+ + O_2$	$\rightleftharpoons$	$O_2^+ + NO$	2.4×10^{13}	0.41	$32,600$
20	$NO^+ + O$	$\rightleftharpoons$	$O_2^+ + N$	7.2×10^{12}	0.29	$48,600$
21	$O^+ + N_2$	$\rightleftharpoons$	$N_2^+ + O$	9.0×10^{11}	0.36	$22,800$
22	$NO^+ + N$	$\rightleftharpoons$	$N_2^+ + O$	7.2×10^{13}	0.0	$35,500$
23	$N + e^-$	$\rightleftharpoons$	$N^+ + e^- + e^-$	2.5×10^{34}	-3.82	$168,700$
24	$O + e^-$	$\rightleftharpoons$	$O^+ + e^- + e^-$	3.9×10^{33}	-3.78	$158,500$

[a] $M_1 = N_2, O_2, NO, N_2^+, O_2^+, NO^+$
[b] $M_2 = N, O, N^+, O^+$
[c] $M_3 = N_2, O_2, N_2^+, O_2^+$
[d] $M_4 = NO, N, O, NO^+, N^+, O^+$

3.2   Thermodynamic properties

Based upon the assumptions mentioned previously, the thermodynamic properties of species i are given by:

for molecules,

$$h_i = \frac{7}{2} R_i T + e_{\text{vib},i} + \Delta h_i^{\text{o}} \tag{3.11}$$

$$e_{\text{vib},i} = R_i \frac{\Theta_{\text{vib},i}}{\exp\left(\Theta_{\text{vib},i}/T\right) - 1} \tag{3.12}$$

$$C_{p,i} = \frac{7}{2} R_i + C_{v,\text{vib},i} \tag{3.13}$$

$$C_{v,\text{vib},i} = R_i \left[\frac{(\Theta_{\text{vib},i}/2T)}{\sinh(\Theta_{\text{vib},i}/2T)} \right]^2 \tag{3.14}$$

for atoms and electrons,

$$h_i = \frac{5}{2} R_i T + \Delta h_i^{\text{o}} \tag{3.15}$$

$$C_{p,i} = \frac{5}{2} R_i \tag{3.16}$$

The values of M_i, $\Theta_{\text{vib},i}$, and Δh_i^{o} are shown in Table 3.2.

3.3   Transport properties

In the present study, transport properties are evaluated by extending Yos' formula [12], which is based on the first Chapman-Enskog approximation, to the single-temperature gas mixture (Refs. [5] and [10]).

Table 3.2: Species data

Species	M_i, kg/mole	$\Theta_{\text{vib},i}$, K	Δh_i^o, J/kg	$E_{\text{D},i}$, J/kg	$E_{\text{I},i}$, J/kg
N_2	28×10^{-3}	$3,353$	0	3.365×10^7	—
O_2	32×10^{-3}	$2,239$	0	1.545×10^7	—
NO	30×10^{-3}	$2,699$	2.995×10^6	2.267×10^7	—
N	14×10^{-3}	—	3.364×10^7	—	1.002×10^8
O	16×10^{-3}	—	1.543×10^7	—	8.218×10^7
N_2^+	28×10^{-3}	$3,129$	5.372×10^7	—	—
O_2^+	32×10^{-3}	$2,652$	3.639×10^7	—	—
NO^+	30×10^{-3}	$3,373$	3.282×10^7	—	—
N^+	14×10^{-3}	—	1.339×10^8	—	—
O^+	16×10^{-3}	—	9.787×10^7	—	—
e^-	5.486×10^{-7}	—	0	—	—

They are written as follows:

Mixture viscosity:

$$\mu = \sum_i \left[\frac{m_i X_i}{\sum_j X_j \Delta_{i,j}^{(2)}(T)} \right] \tag{3.17}$$

Thermal conductivity:

Translational component of thermal conductivity in a mixture excluding electrons:

$$\lambda_{\text{tr}} = \frac{15}{4} k \sum_{i \neq e} \left[\frac{X_i}{\sum_{j \neq e} \alpha_{ij} X_j \Delta_{i,j}^{(2)}(T) + 3.54 X_e \Delta_{i,e}^{(2)}(T)} \right] \tag{3.18}$$

Rotational component of thermal conductivity in a mixture:

$$\lambda_{\text{rot}} = k \sum_{i=M} \left[\frac{X_i}{\sum_j X_j \Delta_{i,j}^{(1)}(T)} \right] \tag{3.19}$$

Vibrational component of thermal conductivity in a mixture:

$$\lambda_{\text{vib}} = k \sum_{i=M} \left[\frac{\left(\dfrac{C_{v\,\text{vib}\,i}}{R_i} \right) X_i}{\sum_j X_j \Delta_{i,j}^{(1)}(T)} \right] \tag{3.20}$$

Thermal conductivity of electrons:

$$\lambda_e = \frac{15}{4} k \frac{X_e}{\sum_{j \neq e} 1.45 X_j \Delta_{e,j}^{(2)}(T) + X_e \Delta_{e,e}^{(2)}(T)} \tag{3.21}$$

Binary diffusion coefficient:

$$\mathcal{D}_{ij} = \frac{kT}{p \Delta_{i,j}^{(1)}(T)} \tag{3.22}$$

where

$$X_i = \frac{\overline{M}}{M_i} C_i \qquad (3.23)$$

$$\Delta_{i,j}^{(1)}(T) = \frac{8}{3} \left[\frac{2m_i m_j}{\pi k T (m_i + m_j)} \right]^{1/2} \pi \overline{\Omega}_{i,j}^{(1,1)} \qquad (3.24)$$

$$\Delta_{i,j}^{(2)}(T) = \frac{16}{5} \left[\frac{2m_i m_j}{\pi k T (m_i + m_j)} \right]^{1/2} \pi \overline{\Omega}_{i,j}^{(2,2)} \qquad (3.25)$$

$$\alpha_{ij} = 1 + \frac{[1 - (m_i/m_j)][0.45 - 2.54(m_i/m_j)]}{[1 + (m_i/m_j)]^2} \qquad (3.26)$$

The collision cross sections $\pi \overline{\Omega}_{i,j}^{(1,1)}$ and $\pi \overline{\Omega}_{i,j}^{(2,2)}$ are the weighted averages of the cross sections for collisions between species i and j, which are defined as

$$\pi \overline{\Omega}_{i,j}^{(l,s)} = \frac{\int_0^\infty \int_0^\pi \exp(-\gamma^2)\gamma^{2s+3}(1 - \cos^l \chi) 4\pi \sigma_{i,j} \sin \chi d\chi d\gamma}{\int_0^\infty \int_0^\pi \exp(-\gamma^2)\gamma^{2s+3}(1 - \cos^l \chi) \sin \chi d\chi d\gamma} \qquad (3.27)$$

where $\sigma_{i,j} = \sigma_{i,j}(\chi, \gamma)$ is the differential scattering cross section for the collision pair i-j, χ the scattering angle in the center-of-mass system, $\gamma = [m_i m_j/(2(m_i + m_j)kT)]^{1/2}g$ the reduced velocity, and g the relative velocity of the colliding particles. They are given by the following function of temperatures in the unit of Å^2 [10].

$$\pi \overline{\Omega}_{i,j}^{(1,1)} = \left[\exp \left(D_{\pi \overline{\Omega}_{i,j}^{(1,1)}} \right) \right] T^{\left[A_{\pi \overline{\Omega}_{i,j}^{(1,1)}} (\ln T)^2 + B_{\pi \overline{\Omega}_{i,j}^{(1,1)}} \ln T + C_{\pi \overline{\Omega}_{i,j}^{(1,1)}} \right]} \qquad (3.28)$$

$$\pi \overline{\Omega}_{i,j}^{(2,2)} = \left[\exp \left(D_{\pi \overline{\Omega}_{i,j}^{(2,2)}} \right) \right] T^{\left[A_{\pi \overline{\Omega}_{i,j}^{(2,2)}} (\ln T)^2 + B_{\pi \overline{\Omega}_{i,j}^{(2,2)}} \ln T + C_{\pi \overline{\Omega}_{i,j}^{(2,2)}} \right]} \qquad (3.29)$$

The coefficients $A_{\pi \overline{\Omega}_{i,j}^{(l,s)}}$, $B_{\pi \overline{\Omega}_{i,j}^{(l,s)}}$, $C_{\pi \overline{\Omega}_{i,j}^{(l,s)}}$, and $D_{\pi \overline{\Omega}_{i,j}^{(l,s)}}$ are given in Tables VIII and IX of Ref. [10].

For the pair of species for which both are ions, the above collision cross sections must be corrected for the given electron pressure p_e by multiplying the following factor:

$$\ln \Lambda(p_e) = \frac{1}{2} \ln \left[2.09 \times 10^{-2} \left(\frac{T}{1000(p_e/101,325)^{1/4}} \right)^4 \right.$$
$$\left. + 1.52 \left(\frac{T}{1000(p_e/101,325)^{1/4}} \right)^{8/3} \right] \qquad (3.30)$$

Effective diffusion coefficient:

According to Curtiss and Hirschfelder [13], in the absence of thermal and pressure diffusions, the diffusion velocity of species i in y-direction is given by

$$V_i^y = -\frac{1 - C_i}{\displaystyle\sum_{j \neq i} X_j/\mathcal{D}_{ij}} \frac{1}{X_i} \frac{\partial X_i}{\partial y} \qquad (3.31)$$

If one defines the effective diffusion coefficient D_i as

$$D_i = \frac{1 - C_i}{\displaystyle\sum_{j \neq i} X_j/\mathcal{D}_{ij}} \frac{\rho_i}{X_i} \qquad (3.32)$$

then the diffusion velocity V_i^y can be expressed as follows:

$$V_i^y = -\frac{D_i}{\rho_i} \frac{\partial X_i}{\partial y} \qquad (3.33)$$

Diffusion coefficient of ions:

Electrons have higher thermal velocities and tend to diffuse faster than ions. A positive charge is then left behind, and an electric field is set up as to deaccelerate electrons and to accelerate ions. Thus, the diffusions of ions and electrons are linked by the electric field. In the present work, this effect is approximately considered by assuming ambipolar diffusion. In this case, the diffusion coefficients for ions can be approximated by

$$D_i^a = 2D_i \tag{3.34}$$

where D_i is the effective diffusion coefficient of ionic species in the absence of electric field.

Diffusion coefficient of electrons:

The effective diffusion coefficient of electrons can be obtained by equating the mass averaged diffusion velocity of ions and that of electrons as follows:

$$D_e = \frac{m_e \sum_{i=I} D_i^a X_i}{\sum_{i=I} m_i X_i} \tag{3.35}$$

4 Method of solution

4.1 Solution for s-momentum, energy, and species conservation equations

As described previously, the s-momentum, energy and species conservation equations are expressed in the standard form for a parabolic partial differential equation, Eq. (2.13). In the present work, a fully implicit scheme is used to march the solution procedure downstream. The discretization of partial derivatives is carried out in the following manner.

With the finite-difference grid shown in Fig. 4.1, the partial derivatives in the η-direction at a grid point (m, n) are discretized using second order central-difference schemes as

$$\left(\frac{\partial W}{\partial \eta}\right)_m^n = a_1 W_m^{n+1} + b_1 W_m^n + c_1 W_m^{n-1} \tag{4.1}$$

$$\left(\frac{\partial^2 W}{\partial \eta^2}\right)_m^n = a_2 W_m^{n+1} + b_2 W_m^n + c_2 W_m^{n-1} \tag{4.2}$$

where

$$a_1 = \frac{\Delta \eta_{n-1}}{\Delta \eta_n (\Delta \eta_n + \Delta \eta_{n-1})} \tag{4.3}$$

$$b_1 = \frac{\Delta \eta_n - \Delta \eta_{n-1}}{\Delta \eta_n \Delta \eta_{n-1}} \tag{4.4}$$

$$c_1 = -\frac{\Delta \eta_n}{\Delta \eta_{n-1} (\Delta \eta_n + \Delta \eta_{n-1})} \tag{4.5}$$

$$a_2 = \frac{2}{\Delta \eta_n (\Delta \eta_n + \Delta \eta_{n-1})} \tag{4.6}$$

$$b_2 = -\frac{2}{\Delta \eta_n \Delta \eta_{n-1}} \tag{4.7}$$

$$c_2 = \frac{2}{\Delta \eta_{n-1} (\Delta \eta_n + \Delta \eta_{n-1})} \tag{4.8}$$

$$\Delta \eta_n = \eta_{n+1} - \eta_n \tag{4.9}$$

The partial derivative in the ξ-direction at (m, n) is approximated by the second order three-points backward difference:

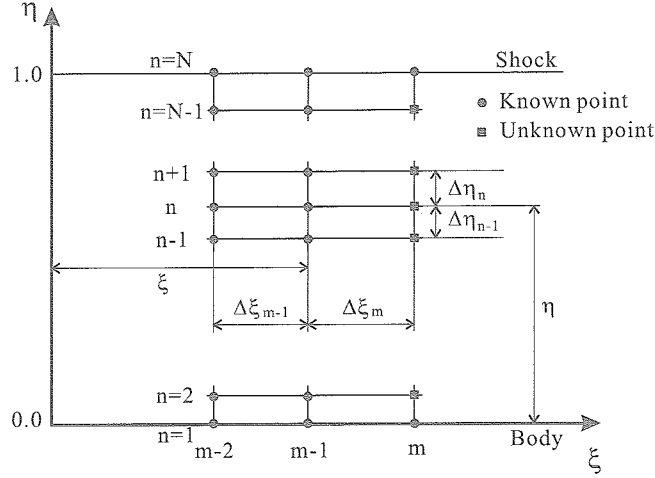$$\left(\frac{\partial W}{\partial \xi}\right)_m^n = d_1 W_m^n + e_1 W_{m-1}^n + f_1 W_{m-2}^n \tag{4.10}$$

Figure 4.1: Schematic of finite-difference grid system

where

$$d_1 = \frac{\Delta\xi_{m-1} + 2\Delta\xi_m}{\Delta\xi_m(\Delta\xi_m + \Delta\xi_{m-1})} \tag{4.11}$$

$$e_1 = -\frac{\Delta\xi_m + \Delta\xi_{m-1}}{\Delta\xi_m \Delta\xi_{m-1}} \tag{4.12}$$

$$f_1 = \frac{\Delta\xi_m}{\Delta\xi_{m-1}(\Delta\xi_m + \Delta\xi_{m-1})} \tag{4.13}$$

$$\Delta\xi_m = \xi_m - \xi_{m-1} \tag{4.14}$$

Substitution of Eqs. (4.1), (4.2), and (4.10) into Eq. (2.13) gives the following simultaneous linear algebraic equations.

$$\widetilde{A}_n W_m^{n-1} + \widetilde{B}_n W_m^n + \widetilde{C}_n W_m^{n+1} = \widetilde{D}_n \tag{4.15}$$

where

$$n = 2, 3, \ldots, n_{\max} - 1 \tag{4.16}$$

$$\widetilde{A}_n = c_2 + A_1^n c_1 \tag{4.17}$$

$$\widetilde{B}_n = b_2 + A_1^n b_1 + A_2^n + A_4^n d_1 \tag{4.18}$$

$$\widetilde{C}_n = a_2 + A_1^n a_1 \tag{4.19}$$

$$\widetilde{D}_n = -A_3^n - A_4^n(e_1 W_{m-1}^n + f_1 W_{m-2}^n) \tag{4.20}$$

This can be efficiently solved using the Thomas algorithm to obtain W_m^n. The detailed description of the Thomas algorithm is found in Ref. [3].

4.2   Shock-layer thickness

The shock-layer thickness is obtained by rearranging the continuity equation which is given previously as

$$\frac{\partial}{\partial\xi}[y_{\text{sh}}(r + y_{\text{sh}}\eta\cos\phi)\rho_{\text{sh}}u_{\text{sh}}\overline{\rho u}] = \frac{\partial}{\partial\eta}[(r + y_{\text{sh}}\eta\cos\phi)\{y'_{\text{sh}}\rho_{\text{sh}}u_{\text{sh}}\overline{\rho u}\eta - (1 + \kappa y_{\text{sh}}\eta)\rho_{\text{sh}}v_{\text{sh}}\overline{\rho v}\}] \tag{4.21}$$

The mass flux between the body ($\eta = 0$) and a given grid point n ($\eta = \eta$) is proportional to m_n (with m_N denoting $\eta = 1$, the shock) which is given by

$$m_n = \int_0^\eta y_{\text{sh}}(r + y_{\text{sh}}\eta\cos\phi)\rho_{\text{sh}}u_{\text{sh}}\overline{\rho u}d\eta \tag{4.22}$$

Integrating Eq. (4.21) from 0 to η and substituting Eq. (4.22) gives another form of the continuity equation

$$\frac{dm_n}{d\xi} = \int_0^\eta \frac{\partial}{\partial \eta} \left[(r + y_{\text{sh}} \eta \cos \phi) \left\{ y'_{\text{sh}} \rho_{\text{sh}} u_{\text{sh}} \overline{\rho u} \eta - (1 + \kappa y_{\text{sh}} \eta) \rho_{\text{sh}} v_{\text{sh}} \overline{\rho v} \right\} \right] d\eta \tag{4.23}$$

or equivalently as

$$\frac{dm_n}{d\xi} = (r + y_{\text{sh}} \eta \cos \phi) \left\{ y'_{\text{sh}} \rho_{\text{sh}} u_{\text{sh}} \overline{\rho u} \eta - (1 + \kappa y_{\text{sh}} \eta) \rho_{\text{sh}} v_{\text{sh}} \overline{\rho v} \right\} \tag{4.24}$$

The shock-layer thickness is obtained by integrating Eqs. (4.22) and (4.23) from 0 to 1 instead of from 0 to η. This gives

$$m_{\text{N}} = y_{\text{sh}} \rho_{\text{sh}} u_{\text{sh}} r \int_0^1 \overline{\rho u} \, d\eta + y_{\text{sh}}^2 \rho_{\text{sh}} u_{\text{sh}} \cos \phi \int_0^1 \overline{\rho u} \eta \, d\eta \tag{4.25}$$

Under the condition of $\eta = 1$ and $\bar{\rho} = \bar{u} = \bar{v} = 1$, Eq. (4.24) becomes

$$\frac{dm_{\text{N}}}{d\xi} = (r + y_{\text{sh}} \cos \phi) \left\{ y'_{\text{sh}} \rho_{\text{sh}} u_{\text{sh}} - (1 + \kappa y_{\text{sh}}) \rho_{\text{sh}} v_{\text{sh}} \right\} \tag{4.26}$$

The term m_{N} of Eq. (4.25) at the location m is obtained by evaluating the right hand side of Eq. (4.26) at each previous location and discretizing the left hand side by the finite difference form given previously as Eq. (4.15), which results in,

$$(m_{\text{N}})_m = [(\text{RHS of Eq. (4.26))}_m - e_1 (m_{\text{N}})_{m-1} - f_1 (m_{\text{N}})_{m-2}] / d_1 \tag{4.27}$$

By substituting this value, we can solve Eq. (4.25) for the shock-layer thickness, y_{sh}.

4.3　Solution for y-momentum and continuity equations

Few problems are encountered in finding solutions to the $s-$momentum, energy and species conservation equations since they are second-order parabolic equations. On the other hand, a difficulty exists in solving the continuity and $y-$momentum equation. This is because these two equations are first-order equations and then we sometimes encounter a so-called even-odd decoupling problem if the first derivatives are evaluated in a central-difference fashion. To alleviate this, in the present code, these two equations are discretized at each $(m, n + 1/2)$ point.

The continuity equation, Eq. (2.28) is rewritten as

$$\frac{\partial A}{\partial \xi} = \frac{\partial}{\partial \eta} [B - C\bar{v}] \tag{4.28}$$

where

$$A = y_{\text{sh}} h_3 \rho_{\text{sh}} u_{\text{sh}} \overline{\rho u}$$
$$B = y'_{\text{sh}} h_3 \rho_{\text{sh}} u_{\text{sh}} \overline{\rho u} \eta$$
$$C = h_1 h_3 \rho_{\text{sh}} v_{\text{sh}} \bar{\rho}$$
$$h_1 = 1 + \kappa y_{\text{sh}} \eta$$
$$h_3 = r + y_{\text{sh}} \eta \cos \phi$$

This is discretized at $(m, n + 1/2)$ points as

$$d_1 A_m^{n+1/2} + e_1 A_{m-1}^{n+1/2} + f_1 A_{m-2}^{n+1/2} = \frac{B_m^{n+1} - B_m^n}{\Delta \eta} - \frac{(C\bar{v})_m^{n+1} - (C\bar{v})_m^n}{\Delta \eta} \tag{4.29}$$

The value of the coefficients at $n + 1/2$ is simply evaluated as an arithmetic average between n and $n + 1$. By rearranging the terms, Eq. (4.29) can be rewritten as

$$a^{n+1/2} \bar{v}_m^{n+1} + b^{n+1/2} \bar{v}_m^n = c^{n+1/2} \tag{4.30}$$

where

$$a^{n+1/2} = C_m^{n+1}/\Delta\eta$$

$$b^{n+1/2} = -C_m^n/\Delta\eta$$

$$c^{n+1/2} = -d_1 A_m^{n+1/2} - e_1 A_{m-1}^{n+1/2} - f_1 A_{m-2}^{n+1/2} + \frac{B_m^{n+1} - B_m^n}{\Delta\eta}$$

Similarly, the difference equation at $(m, n-1/2)$ may be written as

$$a^{n-1/2}\bar{v}_m^n + b^{n-1/2}\bar{v}_m^{n-1} = c^{n-1/2} \tag{4.31}$$

By subtracting Eq. (4.31) from Eq. (4.30), we obtain the equation of tridiagonal form

$$a^{n+1/2}\bar{v}_m^{n+1} + (b^{n+1/2} - a^{n-1/2})\bar{v}_m^n - b^{n-1/2}\bar{v}_m^{n-1} = c^{n+1/2} - c^{n-1/2} \tag{4.32}$$

This can be solved implicitly by using the Thomas algorithm, in the same way as for other second-order parabolic equations.

We can discretize the y-momentum equation in the same way. Equation (2.29) can be rewritten as

$$A + B\frac{\partial(v_{sh}\bar{v})}{\partial\xi} + C\frac{\partial\bar{v}}{\partial\eta} + \frac{\partial\bar{p}}{\partial\eta} = 0 \tag{4.33}$$

where

$$A = -\frac{\kappa y_{sh}\rho_{sh}u_{sh}^2\overline{\rho u^2}}{p_{sh}h_1}$$

$$B = \frac{y_{sh}\rho_{sh}u_{sh}\overline{\rho u}}{p_{sh}h_1}$$

$$C = \frac{\rho_{sh}v_{sh}\bar{p}}{p_{sh}h_1}[h_1 v_{sh}\bar{v} - y'_{sh}u_{sh}\bar{u}\eta] \tag{4.34}$$

Note that ξ derivative of normal velocity is evaluated directly from the nondimensional value $v = v_{sh} \cdot \bar{v}$, not using the expression of $v' = v'_{sh}\bar{v} + v_{sh}\bar{v}'$. Figure 4.2 shows the nondimensional and normalized normal velocity distribution in the vicinity of the body surface ($n = 2$). For the flow field of a hemisphere, there is a location where the dimensional normal velocity component becomes zero. As confirmed from Fig. 4.2, around the region where the normal velocity becomes zero, the normalized velocity component in the normal direction $\bar{v}$ has a sharply varying curve whereas the dimensional normal velocity ($v = \bar{v} \cdot v_{sh}$) shows smooth variation along the body surface. If the three-point backward difference is employed, we suffer from unacceptable numerical errors to evaluate $\partial v/\partial\xi$. Thus the normal velocity streamwise derivative should be discretized directly from v. From numerical experiment, it has been found that this treatment enormously enhances the stability of code.

Equation (4.33) is discretized at $(m, n+1/2)$ as

$$A_m^{n+1/2} + B_m^{n+1/2}\frac{(v_{sh}\bar{v})_m^{n+1/2} - (v_{sh}\bar{v})_{m-1}^{n+1/2}}{\Delta\xi} + C_m^{n+1/2}\frac{v_m^{n+1} - v_m^n}{\Delta\eta} + \frac{p_m^{n+1} - p_m^n}{\Delta\eta} = 0 \tag{4.35}$$

Note that $\partial(v_{sh}\bar{v})/\partial\xi$ is discretized to first-order accuracy. It is also possible to evaluate this term to second-order accuracy, but it has been found that this tends to degrade the convergence speed significantly. From the numerical experiment, it has been confirmed that even evaluating this term to first-order accuracy, we can obtain essentially identical results to the second-order solution.

By rearranging the terms, Eq. (4.35) may be written as

$$a^{n+1/2}\bar{p}_m^{n+1} + b^{n+1/2}\bar{p}_m^n = c^{n+1/2} \tag{4.36}$$

where

$$a^{n+1/2} = 1/\Delta\eta$$

$$b^{n+1/2} = -1/\Delta\eta$$

$$c^{n+1/2} = -A_m^{n+1/2} - B_m^{n+1/2}\frac{(v_{sh}\bar{v})_m^{n+1/2} - (v_{sh}\bar{v})_{m-1}^{n+1/2}}{\Delta\xi} - C_m^{n+1/2}\frac{v_m^{n+1} - v_m^n}{\Delta\eta}$$
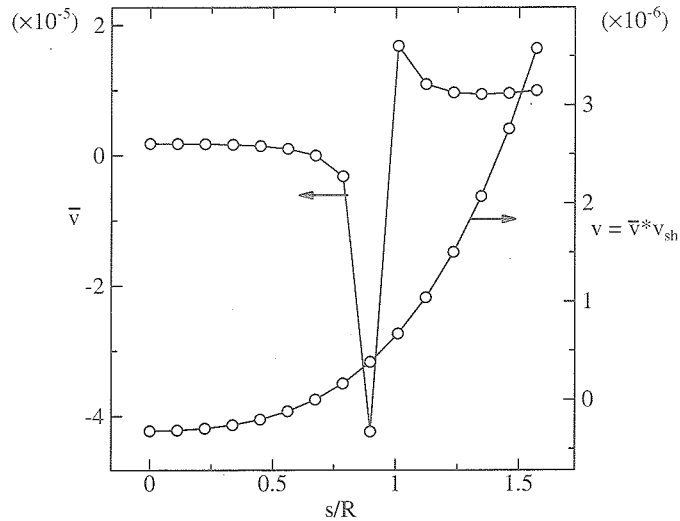
Figure 4.2: Normalized/nondimensional normal velocity distribution
in the vicinity of the body surface

Similarly, the difference equation at $(m, n - 1/2)$ may be written as

$$a^{n-1/2}\bar{p}_m^n + b^{n-1/2}\bar{p}_m^{n-1} = c^{n-1/2} \tag{4.37}$$

By subtracting Eq. (4.37) from Eq. (4.36), we obtain

$$a^{n+1/2}\bar{p}_m^{n+1} + (b^{n+1/2} - a^{n-1/2})\bar{p}_m^n - b^{n-1/2}\bar{p}_m^{n-1} = c^{n+1/2} - c^{n-1/2} \tag{4.38}$$

In the present code, these two equations are solved independently. This is in contrast to the approach employed in another VSL code such as found in Ref. [14], where these two first-order equations are coupled and solved simultaneously to enhance the stability. It has been confirmed that even without solving the two equations in a coupled way, we can obtain a converged solution very stably if only these equations are discretized in the way as described in this section. From the computational point of view, the present approach is apparently much simpler and more efficient.

4.4   The treatment of heat/mass production terms

The production terms concerning chemical reactions appear in the energy equation and the species conservation equations. In the present calculations, to eliminate the strong nonlinearity of the reaction rate, these terms are treated implicitly so that the temperature and mass concentrations appear as one of the unknowns.

For the energy equation, the mass production term at the iteration number $k + 1$ (unknown value) is approximately expressed using values for the iteration number k (known value) as

$$\dot{w}_i^{k+1} = \dot{w}_i^k + \left(\frac{\partial \dot{w}_i}{\partial T}\right)^k (T^{k+1} - T^k) \tag{4.39}$$

Hence the coefficients $\dot{w}_1$ and $\dot{w}_2$ in Eq. (2.27) are written as

$$\dot{w}_1 = \sum_i h_i \left(\dot{w}_i - \frac{\partial \dot{w}_i}{\partial T}T\right) \tag{4.40}$$

$$\dot{w}_2 = \sum_i h_i \frac{\partial \dot{w}_i}{\partial T} \tag{4.41}$$

The derivative $\partial \dot{w}_i/\partial T$ can be evaluated analytically by differentiating Eq. (3.2) with respect to T.

On the contrary, for the species conservation equations, the following expressions are used in Eq. (2.26).

$$\dot{w}_i^0 = M_i \sum_{r=1}^{nr} \left(\Gamma_{i,r}^+ L_{\mathrm{f},r} + \Gamma_{i,r}^- L_{\mathrm{b},r} \right) \tag{4.42}$$

$$\dot{w}_i^1 = \sum_{r=1}^{nr} \left[\Gamma_{i,r}^+ \left(L_{\mathrm{b},r}/\gamma_i \right) + \Gamma_{i,r}^- \left(L_{\mathrm{f},r}/\gamma_i \right) \right] \tag{4.43}$$

$$\Gamma_{i,r}^+ = \begin{cases} (\nu_{i,r}' - \nu_{i,r}), & \text{if } (\nu_{i,r}' - \nu_{i,r}) > 0 \\ 0, & \text{if } (\nu_{i,r}' - \nu_{i,r}) \le 0 \end{cases} \tag{4.44}$$

$$\Gamma_{i,r}^- = \begin{cases} 0, & \text{if } (\nu_{i,r}' - \nu_{i,r}) \ge 0 \\ -(\nu_{i,r}' - \nu_{i,r}), & \text{if } (\nu_{i,r}' - \nu_{i,r}) < 0 \end{cases} \tag{4.45}$$

4.5   Solutions in the stagnation region

The solution begins along the stagnation streamline. When written as in Eq. (4.21), the continuity equation is indeterminate at $\xi = 0$. In order to evaluate the continuity equation at the stagnation point, the following limit expressions as $\xi \to 0$ are used:

$$r \to \xi, \qquad \cos\phi \to \xi, \qquad u_{\mathrm{sh}} \to \xi u_{\mathrm{sh}}'$$

With these expressions, Eq. (4.21) becomes

$$\frac{\partial}{\partial\eta}[(1 + y_{\mathrm{sh}}\eta)^2 \rho_{\mathrm{sh}} v_{\mathrm{sh}} \overline{\rho v}] = -2y_{\mathrm{sh}}(1 + y_{\mathrm{sh}}\eta)\rho_{\mathrm{sh}} u_{\mathrm{sh}}' \overline{\rho u} \tag{4.46}$$

We can readily solve the above equation by applying the same procedure described in the previous section and by replacing the coefficients of Eq. (4.28) as $\partial A/\partial\xi \to 2y_{\mathrm{sh}}h_3\rho_{\mathrm{sh}}u_{\mathrm{sh}}'\overline{\rho u}$, $B \to 0$, and $C \to (1 + y_{\mathrm{sh}}\eta)^2\rho_{\mathrm{sh}}v_{\mathrm{sh}}\overline{\rho}$.

A singularity also exists when solving the s-momentum equation at $\xi = 0$. In order to evaluate A_3 of Eq. (2.16), u_{sh}, $\partial p/\partial\xi$, and y_{sh}' should be expressed in perturbation form as $u_{\mathrm{sh}} \to \xi u_{\mathrm{sh}}'$, $\partial p/\partial\xi \to \xi\partial^2 p/\partial\xi^2$, and $y_{\mathrm{sh}}' \to \xi\partial^2 y_{\mathrm{sh}}/\partial\xi^2$, respectively. Then an alternative expression for A_3 at the stagnation point becomes

$$A_3 = -\frac{y_{\mathrm{sh}}}{\epsilon^2 u_{\mathrm{sh}}'(1 + \kappa y_{\mathrm{sh}}\eta)\mu} \left[y_{\mathrm{sh}}\frac{\partial^2 p}{\partial\xi^2} - \eta\frac{\partial y_{\mathrm{sh}}^2}{\partial\xi^2} \cdot \frac{\partial p}{\partial\eta} \right] \tag{4.47}$$

where the relation of $p = p_{\mathrm{sh}} \cdot \overline{p}$ has been used. It is emphasized here that u_{sh}', $\partial^2 p/\partial\xi^2$, and y_{sh}'' cannot be determined from the stagnation region equations. They are quantities that depend upon the flow downstream. We must therefore assume these values in some appropriate ways. This is further discussed in the next section.

4.6   Shock shape and marching procedure

The VSL algorithms require an initial shock shape as input for the solution method to march in the streamwise direction. In the present code, a simple correlation for blunt-body shock shapes proposed by Billig is employed (Refs. [15] and [16]). The correlations hold for sphere-cone bodies and assume a hyperbolic shock shape given by the following formula

$$z = -\delta + R_c \cot^2\beta \left[\left(1 + \frac{r^2\tan^2\beta}{R_c^2} \right)^{1/2} - 1 \right] \tag{4.48}$$

where R_c is the radius of curvature of the shock wave at the vertex of the hyperbola, δ is the shock standoff distance, and β is the angle of the shock wave in the limit of an infinite distance away from the nose. In

Eq. (4.48), the values of δ and R_c are correlated from experimental data as

$$\frac{\delta}{R_n} = 0.143 \exp\left(\frac{3.24}{M_\infty^2}\right) \tag{4.49}$$

$$\frac{R_c}{R_n} = 1.143 \exp\left[\frac{0.54}{(M_\infty - 1)^{1.2}}\right] \tag{4.50}$$

Although a correlation for perfect gas flows, this gives a sufficiently reasonable initial guess for chemically reacting cases as well. For all of the test cases considered in this paper, converged results were obtained by setting the angle of the shock β to 20 degrees.

The solution for bodies with a spherically blunted nose begins along the stagnation streamline. As noted in the preceding section, to solve VSL equations along the stagnation streamline, three streamwise gradients, namely u'_{sh}, $\partial^2 y_{sh}/\partial\xi^2$, and $\partial^2 p/\partial\xi^2$ are required. The first two of the three can be reduced directly from the analytical expression of the initial shock shape described above. On the other hand, the second derivative of pressure can be approximately evaluated by assuming the following streamwise distribution

$$p = p_1 \cos^2\xi \tag{4.51}$$

where the subscript 1 denotes the stagnation point. Then the second derivative of pressure at the stagnation point is obtained by directly differentiating this expression

$$\left(\frac{\partial^2 p}{\partial\xi^2}\right)_{\xi=0} = (-2p_1\cos\xi)_{\xi=0} = -2p_1 \tag{4.52}$$

Using this expression, the initial flow profile along the stagnation streamline can be obtained.

After the stagnation streamline solution is obtained, the VSL equations are solved at the next downstream location. As the VSL solution is obtained at each local point, it is said that the *local iteration* is completed. At each ξ location, the shock-layer equations are solved in the order: species, energy, s-momentum, y-momentum, and continuity. At each location, the solution is iterated until convergence is obtained for the W's at all points of the finite-difference grid in the η-direction. In the present solution procedure, the underrelaxation method is employed for the local iteration:

$$W_n^{k+1} = \omega W_n^* + (1 - \omega)W_n^k \tag{4.53}$$

where W_n^* is the newly calculated value, W_n^k the previous value, W_n^{k+1} the relaxed value, and ω is the relaxation factor $(0 < \omega < 1)$. The convergence test requires that

$$|1 - W_n^{k+1}/W_n^k| \le 1 \times 10^{-3} \tag{4.54}$$

The calculation is continued successively downstream by using the flow properties of the previous location as an initial guess. When the downstream solution is completed to a specified final location, it is said the first *global iteration* is finished.

In the VSL analysis, the shock-layer thickness y_{sh} is also obtained as a part of the solution. Then the shock shape is updated after each global iterations. In updating the shock shape, the variation of the shock-layer thickness in the streamwise direction is expressed by the 6th-order polynomial expressions as follows

$$y_{sh} = y_{sh0} + \frac{1}{2}y_{sh2}\xi^2 + \frac{1}{4}y_{sh4}\xi^4 + \frac{1}{6}y_{sh6}\xi^6 \tag{4.55}$$

The coefficients y_{sh0}, y_{sh2}, y_{sh4}, and y_{sh6} are determined using the standard least-square curve fitting method together with the shock-layer thickness data obtained from the previous global iteration. The coefficient y_{sh2} in Eq. (4.55) corresponds to the second derivative of y_{sh} and is used to solve the continuity equation at the stagnation point. The shock angle α is obtained from

$$\alpha = \theta + \tan^{-1}\left[\frac{y'_{sh}}{1 + \kappa y_{sh}}\right] \tag{4.56}$$

```
┌─────────────────────┐
│ Initially obtain shock shape
│ from Billig's correlation
└─────────────────────┘
          ↓
┌─────────────────────┐
│ Calculate shock properties
│ and streamwise derivatives  ←────┐
│ from the shock shape        │
└─────────────────────┘         │
          ↓ m= 1                  │
┌─────────────────────┐  m=m+1   │
│ Solve VSL equations at m ←──┐   │
└─────────────────────┘      │   │
          ↓                   │   │
      Check local             │   │
   No  convergence            │   │
  ←───                        │   │
          ↓ Yes               │   │
      m = mmax                │   │
              No ────────────┘   │
          ↓ Yes                   │
┌─────────────────────┐          │
│ Update shock shape using        │
│ shock-layer thickness           │
│ obtained                        │
└─────────────────────┘          │
          ↓                       │
      Check global                │
   convergence   No ─────────────┘
          ↓ Yes
        ( End )
```
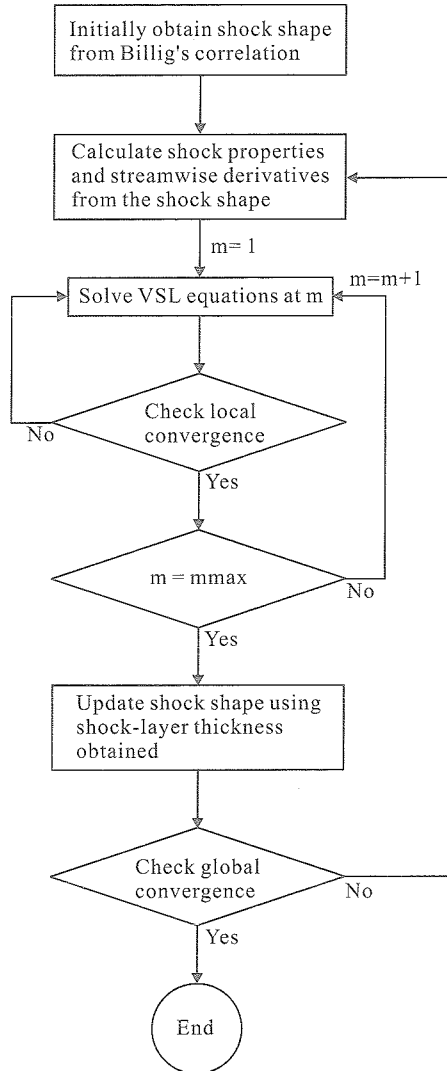
Figure 4.3: Solution flowchart

where $y'_{sh} = dy_{sh}/d\xi$ is evaluated by differentiating Eq. (4.55) with respect to ξ. From the values of shock angle obtained at each local point, new flow properties behind the shock wave and streamwise gradients of the shock properties can be computed. The newly obtained y'_{sh} and α are underrelaxed using the previous values and a relaxation parameter of $\omega = 0.5$ was used for all of the test cases considered in this paper. From the second global iteration, the second derivative of pressure at the stagnation point 1 can be numerically evaluated from the quantities next to the stagnation streamline and considering the flow symmetry conditions as

$$\left(\frac{\partial^2 p}{\partial \xi^2}\right)_1 = 2\frac{p_2 - p_1}{\Delta \xi_1^2} \tag{4.57}$$

where subscript 2 represent the point next to the stagnation. The global iteration procedure is repeated until the shock layer thickness converges sufficiently.

Finally, the overall solution flowchart of the present VSL analysis is illustrated in Fig. 4.3.

5   Code description

The specification of the present code is summarized in Table 5.1. The code is written in C language and developed under the environment of a personal computer with Borland C++ 5.5 as a compiler. At present, the present code is suitable only for a hemisphere. Although it is possible to apply the present code

Table 5.1: Specification of the present code

Language	C
Species/reactions	air 5 species (N_2, O_2, NO, N, O), 17 reactions
	air 7 species (N_2, O_2, NO, N, O, NO^+, e^-), 22 reactions
	air 11 species (N_2, O_2, NO, N, O, NO^+, N_2^+, O_2^+, N^+, O^+, e^-), 48 reactions
	nitrogen 2 species (N_2, N), 2 reactions
	nitrogen 5 species (N_2, N, N_2^+, N^+, e^-), 8 reactions
Thermal state	equilibrium (one temperature model)
Reaction rates	Park [9]
Transport properties	Gupta [10]
Wall temperature	fixed/radiative equilibrium condition
Wall catalysis	NCW/FCW/finite rate

to arbitral body geometries (e.g. hyperboloid or sphere-cone), there might be a case where an additional control parameter is required to obtain converged solutions. It should be emphasized that one philosophy of the present code is to minimize the user interaction to make the computational procedure much simpler even at the expense of generality. Dynamic allocation of the array is possible, so that the user can change the number of grid points arbitrarily. However, it is well known that the stability of a space-marching scheme strongly depends on the size of the streamwise step size $\Delta\xi$. This is because, in the VSL method, the pressure gradient term in the streamwise momentum equation is approximated as a hyperbolic term through backward differences in the subsonic nose region [17]. To alleviate convergence problems, it is recommended that the step size $\Delta\xi$ should be more than 0.1 (non-dimensional value) in the subsonic region. In the present code, 15 grid points are equally placed along the body surface (corresponding to $\Delta\xi = 0.105$) at default. On the other hand, the number of grid points in the normal direction can be specified arbitrarily without any problems. The user can select two gas species (air and nitrogen) and can solve the flow field both for perfect and chemically reacting gas cases. The species number can be selected from the three sets (5, 7, and 11 species) for air and two sets (2 and 5 species) for nitrogen, respectively. Every species/reaction model is a subset of the original air 11-species, 48-reactions model (see Table 3.1). The shock-slip effects are not included at present.

6 Code validation

6.1 Comparison to other VSL/NS computations for perfect gas flows

The present VSL code is first compared with a Navier-Stokes code for calorically perfect gas cases. The Navier-Stokes code was also developed by the present author and is briefly described below.

The governing equations employed are the axi-symmetric Navier-Stokes equations assuming laminar and calorically perfect gas flow. The viscosity and thermal conductivity are evaluated using Yos' formula which is the same as given in the preceding section. The code employs a shock-capturing scheme and the governing equations are discretized using a finite volume approach. A cell-vertex scheme is employed, so that all flow properties are defined at the node of each grid point. The inviscid flux at the cell boundary is evaluated using the AUSM-DV scheme [19]. The space accuracy is kept up to second-order by the MUSCL type interpolation technique [20]. Time integration is performed implicitly by applying the LU-SGS algorithm [21].

The comparison was made for typical flow conditions of a blow-down type hypersonic wind tunnel. The free stream Mach number, temperature, density are 9.55, 55.5 K, and 4.81×10^{-3} kg/m^3, respectively. The body nose radius is set to 3 cm and a fixed temperature of 300 K is imposed on the body surface. In Fig. 6.1, the pressure contours obtained from the VSL computation are overlapped on the result of the NS computation. It is obvious that the present VSL code gives essentially identical results compared with the NS solver. The shock shape obtained as a part of the solution in the VSL analysis agrees very well

Table 6.1: Freestream conditions (taken from Ref. [23])

M	5	5	5	10	10	10	15	15	15
Re	10^3	10^4	10^5	10^3	10^4	10^5	10^3	10^4	10^5
T_∞ (K)	212	212	212	212	212	212	212	212	212
p_∞ (Pa)	1.277	12.77	127.7	1.916	19.16	191.6	3.832	38.32	383.2
u_∞ (m/s)	4393	4393	4393	2928	2928	2928	1464	1464	1464
T_w (K)	212	212	212	1500	1500	1500	1500	1500	1500

Table 6.2: VSL-NS comparisons for stagnation heat flux/pressure

Stagnation point heat flux (kW/m^2)

M	5	5	5	10	10	10	15	15	15
Re	10^3	10^4	10^5	10^3	10^4	10^5	10^3	10^4	10^5
VSL	11.0	34.0	106.4	48.5	147.3	459.4	192.3	566.7	1751.7
NS	11.0	33.8	106.2	48.8	146.6	454.9	190.0	563.6	1740.9
VSL-NS (%)	0.5	0.7	0.2	-0.6	0.4	1.0	1.2	0.6	0.6

Stagnation point pressure (Pa)

M	5	5	5	10	10	10	15	15	15
Re	10^3	10^4	10^5	10^3	10^4	10^5	10^3	10^4	10^5
VSL	125.4	1251.5	12513.0	248.5	2476.7	24758.8	373.4	3708.4	37056.6
NS	125.5	1251.3	12505.5	249.0	2470.9	24707.1	375.5	3702.8	36986.7
VSL-NS (%)	-0.1	0.0	0.1	-0.2	0.2	0.2	-0.6	0.2	0.2

with the shock captured by the Navier-Stokes solver. The nondimensionalized wall heat flux distributions as a function of body half apex angle θ are compared between two results in Fig. 6.2 together with the theoretical distributions of Lees [22]. Even in this case, these two results are almost identical. As a next step, the comparison was made over a wide range of Reynolds and Mach numbers. The calculations are carried out for a total of nine free stream conditions with three levels of Mach numbers ($M = 5, 10, 15$) and corresponding three levels of Reynolds numbers ($Re = 10^3, 10^4, 10^5$). The detailed free stream conditions are given in Table 6.1. These conditions are taken from the work of Müler et al. [23] A hemisphere with nose radius of 0.1524 m was considered.

Table 6.2 summarizes the stagnation point heat flux and pressure obtained from the present computations. Both for the stagnation point heat flux and pressure, the results of the VSL and NS agree very well for every condition. In addition, the results of the present work agree well even in very low Reynolds number cases. Therefore it has been confirmed that the present VSL code has a sufficient accuracy compared to the Navier-Stokes solver.

6.2   Comparison to the JAXA 1.27 m hypersonic wind tunnel experimental data

Next results yielded from the present code are compared with existing experimental data obtained at a cold-type hypersonic wind tunnel. In the National Aerospace Laboratory of Japan (NAL), which is a predecessor institute of the Japan Aerospace Exploration Agency (JAXA), a series of heat flux measurements were performed at the 1.27 m hypersonic wind tunnel (HWT). The schematic view of HWT is shown in Fig. 6.3. HWT is a blow-down type cold wind tunnel with nominal Mach number of 10. The stagnation enthalpy is approximately 1 MJ/kg and available unit Reynolds numbers range from 1.0×10^6 to 4.3×10^6 /m. To avoid liquefaction of air, a pebble bed heater heated by a line gas burner is utilized. The humidity management system including the combustion gas replacement system keeps the humidity in the working gas below 50 ppmV at a reservoir pressure of 4 MPa. Previously conducted flow calibration tests confirmed the Mach number uncertainty is less than 0.3 % in the core flow part.

The model employed in the experiment is called HB-2 type model which is a standard model proposed in
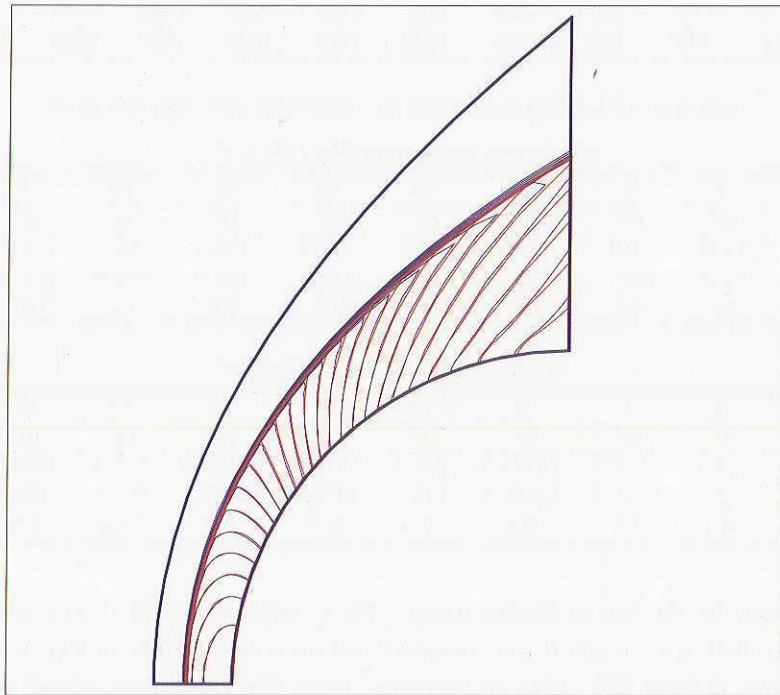
Figure 6.1: Pressure contours comparison between the VSL (red line)
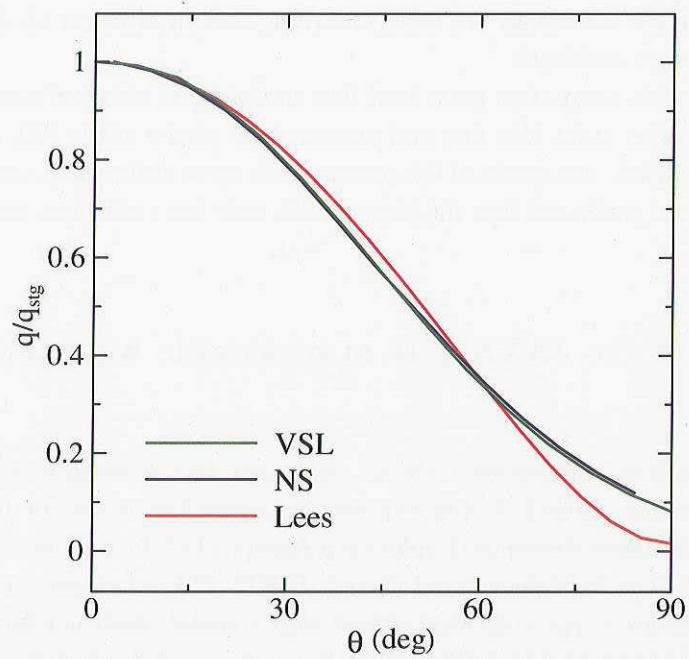and the Navier-Stokes (blue line) solutions

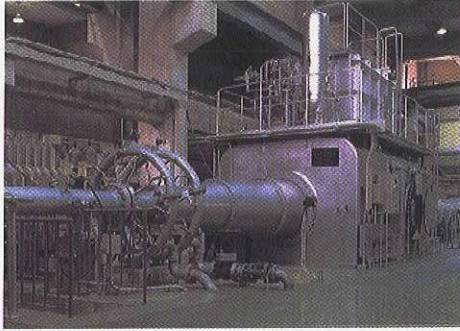Figure 6.2: Comparison of nondimensional wall heat flux distributions

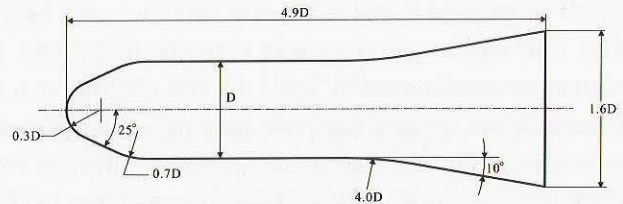Figure 6.3: JAXA 1.27 m Hypersonic Wind Tunnel (HWT)

Figure 6.4: HB2 model

Table 6.3: Comparison to the HWT experimental data

Run No.	P_0 (MPa)	M	ρ_∞ (kg/m^3)	T_∞ (K)	Re	ϵ	q_{stg} (kW/m^2)		
							Exp.	VSL	VSL-Exp (%)
1322	6	9.66	1.05×10^{-2}	57.1	1.22×10^5	0.003	232.1	239.5	3.21
1324	4	9.62	7.52×10^{-3}	54.3	9.05×10^4	0.003	177.9	181.8	2.18
1323	2.5	9.55	4.81×10^{-3}	55.5	5.67×10^4	0.004	144.0	147.4	2.38
1327	2.5	9.55	4.95×10^{-3}	54.3	5.92×10^4	0.004	142.5	143.2	0.48
1328	2.5	9.55	4.85×10^{-3}	55.0	5.74×10^4	0.004	143.3	145.6	1.56
1329	2.5	9.54	4.78×10^{-3}	56.3	5.57×10^4	0.004	148.0	150.4	1.58
1330	2.5	9.54	4.82×10^{-3}	56.0	5.63×10^4	0.004	146.7	149.3	1.76
1331	2.5	9.55	4.94×10^{-3}	54.1	5.92×10^4	0.004	140.9	142.3	0.98
1332	2.5	9.55	4.88×10^{-3}	54.7	5.81×10^4	0.004	142.3	144.3	1.41
1333	2.5	9.56	4.90×10^{-3}	54.3	5.86×10^4	0.004	140.2	142.8	1.90
1334	2.5	9.55	5.03×10^{-3}	53.3	6.09×10^4	0.004	137.6	139.1	1.06
1339	2.5	9.55	4.80×10^{-3}	55.8	5.62×10^4	0.004	144.2	148.5	2.98
1340	2.5	9.55	4.95×10^{-3}	54.0	5.95×10^4	0.004	139.8	141.7	1.33
1341	2.5	9.55	4.92×10^{-3}	54.4	5.87×10^4	0.004	140.6	143.2	1.84
1343	2.5	9.56	5.01×10^{-3}	53.4	6.06×10^4	0.004	137.9	139.5	1.16
1346	1	9.41	2.33×10^{-3}	50.9	2.86×10^4	0.006	83.0	81.8	-1.47
1348	1	9.40	2.27×10^{-3}	52.3	2.74×10^4	0.006	84.9	85.0	0.10

Re is based on the centerbody diameter of the model (100 mm)

a joint program of AGARD and Supersonic Tunnel Association (STA) in 1950–60's [25]. It has an analytical shape which consists of sphere, cone, cylinder, and flare as shown in Fig. 6.4. In this model, a total of 28 chromel-constantan type co-axial thermocouples of 1.5 mm diameter are press-fitted. The experiment was conducted at stagnation pressures of 1, 2.5, 4, and 6 MPa. For each stagnation pressures, the stagnation enthalpy is approximately 1 MJ/kg. The corresponding Reynolds numbers based on the model centerbody diameter are 1.0, 2.0, 3.0, and 4.3×10^5, respectively. More detailed description of the experiment is found in Ref. [26].

In Table 6.3, the stagnation heat flux values obtained from the VSL computations are compared with the experimental data. The VSL results agree reasonably with the experimental data for every condition. There is a tendency that the difference between the experimental data becomes larger as the stagnation point pressure P_0 becomes higher. This is probably because the intermolecular effects of the stagnation gas in the reservoir becomes significant as P_0 becomes higher. In this case, it might be inadequate to calculate the free stream conditions from the one-dimensional isentropic conditions plus the real gas correction formula proposed in Ref. [27].

6.3   Computations at the OREX flight conditions

A series of computations has been performed for the reentry flow field around the forebody of the Japanese Orbital Reentry Experiment (OREX) vehicle. This vehicle has a 50-deg spherically blunted cone

with a nose radius of 1.35 m and a base diameter of 3.4 m. Calculations were done for the OREX trajectory from 60 to 97 km altitude range. The free stream conditions are tabulated in Table 6.4. The 11 species model is employed and both non catalytic and fully catalytic wall boundary conditions are considered. The VSL results are compared with the flight data and the Navier-Stokes results of Kurotaki [28]. The results are summarized in Table 6.5 and illustrated in Fig. 6.5. Although a slight difference can be observed for conditions around the peak heating region, the agreement between the present and the NS results is satisfactory. On the other hand, at higher altitudes (i.e., low Reynolds numbers), the VSL method predicts much higher heat flux values than expected due to the neglect of the higher order terms.

Table 6.4: Free stream conditions of Orbital Reentry Experiment (OREX) trajectory (taken from Ref. [18])

Case	Time (sec)	Altitude (m)	U_∞ (m/s)	ρ_∞ (kg/m³)	T_∞ (K)	M	T_w (K)
1	7381.0	96.77	7456.3	1.3810×10^{-6}	192.0	26.72	485.0
2	7391.0	92.82	7454.1	3.0090×10^{-6}	189.0	26.97	586.0
3	7401.0	88.45	7444.3	4.3060×10^{-6}	187.0	27.07	687.0
4	7411.5	84.01	7415.9	1.0953×10^{-5}	189.0	26.82	785.0
5	7421.5	79.90	7360.2	1.8455×10^{-5}	199.0	26.82	878.0
6	7431.5	75.81	7245.7	3.6576×10^{-5}	207.0	25.04	976.0
7	7441.5	71.73	7049.2	6.5184×10^{-5}	215.0	23.89	1091.0
8	7451.5	67.66	6720.3	1.2164×10^{-4}	226.0	22.22	1213.0
9	7461.5	63.60	6223.4	2.0594×10^{-4}	237.0	20.09	1344.0
10	7471.5	59.60	5561.6	3.3131×10^{-4}	248.0	17.55	1458.0

Table 6.5: Comparison of the wall heat flux for the conditions of OREX

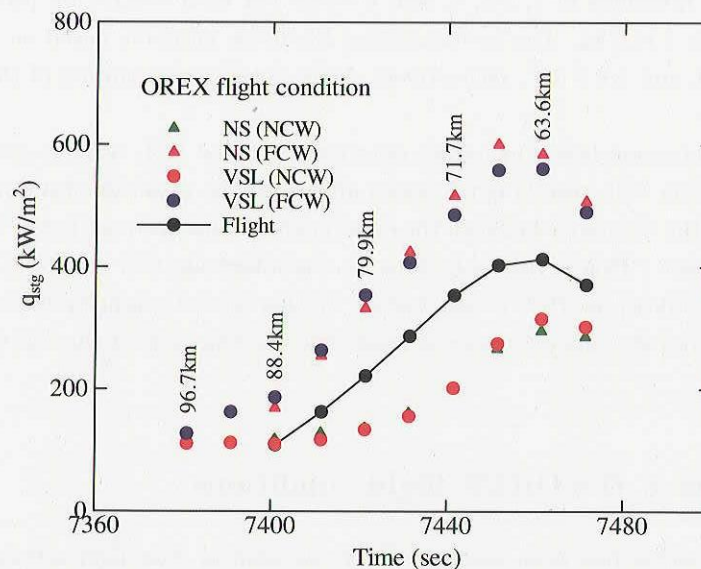| Case	q_{stg} (kW/m²)				
	VSL		NS [28]		Flight
	NCW	FCW	NCW	FCW	
1	110.6	127.1	–	–	–
2	111.7	162.3	–	–	–
3	110.3	186.5	117.3	168.6	109.0
4	117.0	263.4	128.0	254.1	163.0
5	133.6	353.9	136.0	331.8	222.0
6	155.5	407.3	160.4	423.9	287.0
7	201.8	485.1	200.3	516.1	354.0
8	274.4	558.5	266.0	600.1	403.0
9	314.9	560.8	295.1	584.1	413.0
10	301.7	489.9	285.6	506.6	371.0

Figure 6.5: Comparison of the wall heat flux for the conditions of OREX

6.4 Computations at the AFE flight conditions

Next the results are presented for the stagnation point heat flux for a wide range of flight conditions of the Aeroassist Flight Experiment (AFE), a project that NASA initiated to gather flight data in the flight regime that would be typical for future aeroassist missions, and are compared with the VSL solutions performed by Gupta [29]. The configuration of the AFE vehicle forebody is a full three-dimensional ellipsoidal nose tangent to an elliptical cone, but an axially symmetric representation of the AFE, consisting of a spherical segment nose with an effective nose radius of 2.16 m was considered here. This effective nose radius was selected according to Ref. [29], where the resultant convective heating prediction at the peak heating condition using this radius was found to be the same as that calculated by the benchmark LAURA code for the full three-dimensional configuration at an angle of attack of 0 degrees.

The free stream conditions for the present calculations are taken from the AFE trajectory and summarized in Table 6.6. In Ref. [29], Gupta et al. performed a series of computations using their VSL code which employed a 5-species chemical reaction model assuming thermal equilibrium. Finite rate catalysis is assumed on the body surface. The transport properties used are consistent with the present code. At higher altitudes of AFE, the flow may be too rarefied to justify the simplifying assumptions of the VSL method, so that the Navier-Stokes computations including the wall-slip effects were also performed.

For the purpose of comparison, in the present calculation, the 5-species model was employed. The wall catalysis model used is the same as in Ref. [29] and described in Section 2.3. Computations for both the NCW and FCW conditions were also performed. The wall temperature is estimated by assuming the radiative equilibrium condition with a surface emissivity of 0.85. An estimate of the nonequilibrium radiative heat transfer rate has also been included to estimate the wall temperature using the correlation formula found in Ref. [30].

The comparison of the stagnation heat flux and the wall temperature between the present results and the data of Ref. [29] is summarized in Table 6.7 and illustrated in Fig. 6.6. As can be seen from the table, at lower altitudes, a strong influence of wall catalysis is observed. Hence the accuracy of the heat flux estimation for finite rate catalytic wall conditions is very sensitive to the accuracy of the species mass concentrations in the vicinity of the wall. Even considering these facts, for every case, favorable agreement with the VSL solutions of Ref. [29] is achieved for lower altitude cases. On the other hand, at higher altitudes, the VSL solution does not give reasonable results any more due to the perturbation error.

Table 6.6: Free stream conditions of Aeroassist Flight Experiment (AFE) trajectory (taken from Ref. [29])

Case	Time (sec)	Altitude (km)	U_∞ (m/s)	ρ_∞ (kg/m^3)	p_∞ (Pa)	T_∞ (K)	M
1	0.0	121.9	9894	1.973×10^{-8}	2.465×10^{-3}	435.3	24.15
2	9.6	114.4	9905	5.028×10^{-8}	4.740×10^{-3}	328.5	27.89
3	19.2	107.5	9911	1.468×10^{-7}	1.077×10^{-2}	255.6	31.51
4	28.8	101.3	9915	4.379×10^{-7}	2.471×10^{-2}	196.6	34.30
5	38.4	95.7	9917	1.245×10^{-6}	6.815×10^{-2}	190.7	36.03
6	49.9	89.9	9909	3.665×10^{-6}	1.944×10^{-1}	184.8	36.39
7	59.5	85.8	9888	7.285×10^{-6}	3.999×10^{-1}	191.3	35.67
8	69.1	82.4	9844	1.278×10^{-5}	7.125×10^{-1}	194.3	35.21
9	78.7	79.9	9769	1.961×10^{-5}	1.102×10^{0}	195.8	34.78
10	88.3	78.2	9665	2.597×10^{-5}	1.468×10^{0}	197.0	34.31
11	97.9	77.3	9537	3.035×10^{-5}	1.722×10^{0}	197.7	33.80
12	107.5	76.6	9395	3.388×10^{-5}	1.927×10^{0}	198.2	33.26
13	117.1	76.1	9244	3.684×10^{-5}	2.099×10^{0}	198.5	32.70
14	126.7	75.7	9087	3.916×10^{-5}	2.235×10^{0}	198.9	32.12
15	136.3	75.5	8927	4.084×10^{-5}	2.333×10^{0}	199.0	31.54
16	145.9	75.3	8767	4.220×10^{-5}	2.413×10^{0}	199.2	30.97
17	155.5	75.2	8609	4.253×10^{-5}	2.433×10^{0}	199.3	30.40

Table 6.7: Comparison of the wall heat flux and the wall temperature for the conditions of AFE

| Case | VSL (Present) | | | | | | VSL [29] | | NS [29] | |
| | NCW | | Finite rate | | FCW | | Finite rate | | Finite rate | |
	q_{stg} (kW/m^2)	T_w (K)	q_{stg} (kW/m^2)	T_w (K)	q_{stg} (kW/m^2)	T_w (K)	q_{stg} (kW/m^2)	T_w (K)	q_{stg} (kW/m^2)	T_w (K)
1	145.2	1318	145.2	1318	145.6	1319			8.7	652
2	148.6	1326	148.5	1326	149.1	1327			20.3	806
3	149.9	1330	150.6	1331	152.9	1336			44.4	982
4	120.6	1262	128.8	1283	140.5	1311			81.4	1154
5	110.7	1246	130.1	1295	191.0	1421			116.6	1260
6	107.8	1262	159.2	1378	272.2	1562	153.1	1360	142.8	1344
7	125.7	1335	213.2	1495	355.7	1679	227.4	1510		
8	155.1	1428	288.7	1623	445.9	1787	310.7	1642		
9	191.6	1519	366.6	1730	531.5	1876	354.5	1711		
10	219.4	1578	421.9	1796	591.3	1931	386.5	1756		
11	226.8	1594	443.5	1819	610.8	1949	401.4	1775		
12	224.8	1592	449.7	1825	611.1	1949	408.8	1782		
13	217.8	1580	442.4	1817	599.5	1940	410.8	1782		
14	208.2	1561	428.7	1801	580.1	1923	408.8	1776		
15	197.7	1539	409.5	1778	555.2	1900	407.0	1766		
16	189.2	1518	390.4	1755	530.7	1877	396.4	1754		
17	178.3	1492	367.9	1726	501.1	1848	386.2	1738		
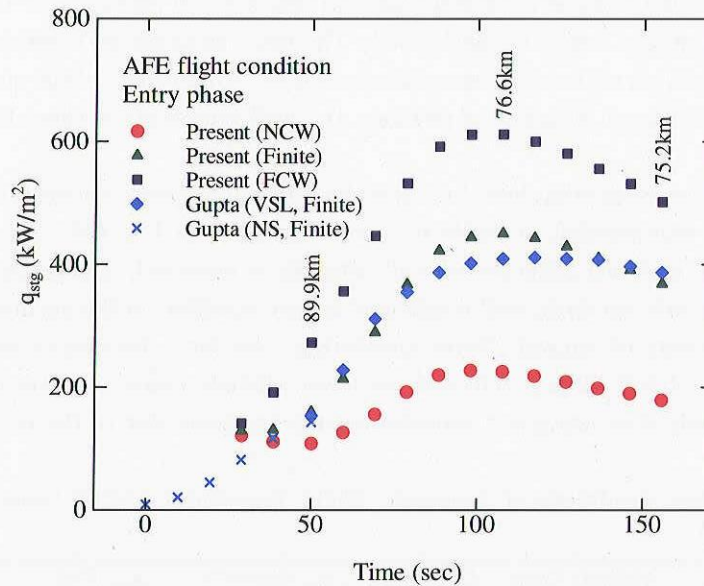
Figure 6.6: Comparison of the wall heat flux for the conditions of AFE

6.5   Computation at the ONERA F4 high enthalpy wind tunnel condition

The simulation was also performed at the condition of the ONERA F4 high enthalpy wind tunnel under the assumptions of fully catalytic wall. The free stream conditions are taken from Ref. [34] and shown in Table 6.8. The wall temperature is fixed to 300 K and the result is compared with the Navier-Stokes code CELHYO. The detailed description of CELHYO is found in Ref. [32]. In Table 6.8, the stagnation heat flux and the shock standoff distance obtained from the present VSL code are compared with the data taken from Ref. [34]. A favorable agreement is confirmed for the stagnation heat flux, whereas considerable difference can be found for the shock-layer thickness. This discrepancy probably comes from the difference of the chemical models employed.

Table 6.8: Free stream conditions of the ONERA F4 high enthalpy wind tunnel and comparison of the numerical results

ρ_∞ (g/m^3)	p_∞ (Pa)	T_∞ (K)	M_∞	u_∞ (m/s)	q_{stg} (MW/m^2) Present	CELHYO	y_{sh}/R_n Present	CELHYO
0.82068	191.8	810.7	8.8	5010	4.22	4.40	0.0818	0.0937

Table 6.9: HEG standard operating conditions (conical nozzle)

Cond.	I	II	III	IV
p_0 (MPa)	35	85	44	90
T_0 (K)	9100	9900	7000	8100
h_0 (MJ/kg)	22	23	12	15
p_∞ (Pa)	660	1700	790	1680
T_∞ (K)	1140	1450	800	1060
ρ_∞ (g/m^3)	1.7	3.5	3.3	5.3
M_∞	8.2	7.8	8.1	7.9
u_∞ (km/s)	5.9	6.2	4.7	5.2

Table 6.10: VSL results of stagnation pressure and heat flux for the HEG standard operating conditions ($R_n = 10\,\text{mm}$)

Cond.	Wall catalysis	Species	p_{stg} (kPa)	q_{stg} (MW/m^2)	q_{stg} (MW/m^2) (Eq. 6.1)
I	NCW	5	502.6	13.59	
		7	502.6	13.66	
		11	502.6	13.66	15.95
	FCW	5	502.7	16.12	
		7	502.7	16.16	
		11	502.7	16.18	
II	NCW	5	119.9	24.38	
		7	119.9	24.46	
		11	119.9	24.47	28.92
	FCW	5	119.9	27.65	
		7	119.9	27.67	
		11	119.9	27.72	
III	NCW	5	66.6	8.59	
		7	66.6	8.61	
		11	66.6	8.61	12.16
	FCW	5	66.6	12.02	
		7	66.6	12.04	
		11	66.6	12.03	
IV	NCW	5	135.7	16.88	
		7	135.7	16.91	
		11	135.7	16.91	22.45
	FCW	5	135.7	21.40	
		7	135.7	21.42	
		11	135.7	21.43	

6.6 Computations at the DLR HEG standard conditions

A series of computations has been performed concerning the four standard operating conditions of the High Enthalpy Shock Tunnel Göttingen (HEG). A detailed description of the facility is given in Refs. [36] and [37]. The cataloged operating conditions are summarized in Table 6.9. The effect of free stream dissociation is not taken into account at present, so that the total enthalpy specified is much lower than actual. As for the surface catalysis, both non-catalytic and full catalytic wall conditions were considered. The wall temperature was fixed to 300 K. A total of three sets of chemical species (5, 7, and 11 species) were taken into account and the results were compared. The body nose radius was set to 10 mm, the same as the radius of the heat flux permanent probe installed in the HEG test section. The stagnation heat flux obtained was also compared with the correlation formula proposed by the group of ONERA. Verant developed a correlation based upon Navier-Stokes computations for perfect and nonequilibrium flows with the enthalpy ranging up to 24 MJ/kg. This correlation was developed to determine the total enthalpy of the flow measured from the Pitot pressure and stagnation point heat flux probes in the F4 facility. The empirical correlation is given as

$$q_w = 23.787 \sqrt{\frac{p_t}{R_n}} \left(\frac{h_0 - h_w}{RT_{ref}} \right)^{1.0688} \tag{6.1}$$

where $R = 280.015\,\text{J/(kgK)}$ is the gas constant and $T_{ref} = 273.15\,\text{K}$ is the reference temperature. The detail of the correlation is found in Refs. [31] and [33]. Equation (6.1) was used to compare with the present VSL results. To estimate the stagnation heat flux from Eq. (6.1), the stagnation enthalpy h_0 was directly taken from the values of Table 6.9, whereas the values obtained from the VSL computations were substituted for the stagnation pressure p_t. The results are tabulated in Table 6.10. For every condition, both the stagnation

Table 6.11: Nozzle reservoir conditions of the present HEG runs

Run	Cond.	Gas	p_0 (MPa)	T_0 (K)	H_0 (MJ/kg)
627	III	Air	48.3	7369	13.5
615	III	N_2	53.0	8480	11.9
619	I	Air	35.0	9200	22.4
625	I	N_2	34.8	9625	19.5

Table 6.12: Free stream conditions of the present HEG runs

Run	ρ_∞ (g/m^3)	p_∞ (Pa)	T_∞ (K)	M_∞	Mass fraction				
					N_2	O_2	NO	N	O
627	3.255	687	694	8.78	0.7356	0.1340	0.0509	0.0000	0.0796
615	2.755	500	610	10.0	0.9891	–	–	0.0109	–
619	1.547	476	901	8.98	0.7543	0.0070	0.0102	0.0000	0.2284
625	1.361	452	1060	8.87	0.9356	–	–	0.0644	–

Table 6.13: Comparison to the HEG experimental data

Run	Cond.	Gas	q_{stg} (MW/m^2)			
			VSL		Exp.	Eq. (6.1)
			NCW	FCW		
627	III	Air	11.38	15.30	14.5	14.68
615	III	N_2	15.34	15.44	14.2	
619	I	Air	20.69	23.34	20.8	22.23
625	I	N_2	21.58	22.80	20.1	

pressure and the heat flux are essentially invariant with respect to the number of chemical species. Hence the 5-species model is found to be enough to estimate these properties at the HEG conditions. The agreement of the heat flux between the present VSL computation for the FCW condition and the values obtained from Eq. (6.1) is confirmed to be reasonable as well.

6.7   Comparison to the HEG experimental data

In Ref. [35], a test campaign of the flow around a cylinder has been performed in the HEG. The present data have been obtained using a conical nozzle with throat and exit radii of 0.011 m and 0.44 m, respectively. The half angle of the nozzle is approximately 6.5°. The experiments were performed at the HEG conditions I (high enthalpy) and III (medium enthalpy) with either air or nitrogen as test gas. The free stream conditions of each run were evaluated by the nonequilibrium nozzle flow computation together with the reservoir conditions obtained from the 1D simulation and a suitable set of measured parameters. The detailed description of the analysis is found in Ref. [35]. The reservoir and free stream conditions for the corresponding HEG runs are summarized in Tables 6.11 and 6.12, respectively. In the experiments, three permanent probes are mounted which monitor the Pitot pressure, the stagnation point heat flux on a hemisphere, and the static pressure in the free stream. The radius of the heat flux permanent probe is 10 mm. In the present VSL analysis, the flow field around the heat flux permanent probe has been solved. The surface was assumed to be fully catalytic and the number of chemical species was taken to be 7 species for air and 2 species for nitrogen flow, respectively.

In Table 6.13, the stagnation heat flux at each run are compared between the VSL results and the experimental data. For runs 627 and 619 (air as test gas), the heat flux values obtained from Eq. (6.1) are also presented. For FCW conditions, the VSL results predict approximately 10 % higher heat flux compared to experimental data. This discrepancy is presumably due to uncertainties coming from the determination of the free stream conditions and the data reduction process of the experimental data. Uncertainty concerning the depth of the thermocouple probe junction is another possibility. It has been pointed out that more than 30 % of uncertainty can be caused for short duration test facilities if the thermocouple junction is made

Table 6.14: List of iteration numbers and CPU times with conditions of the HOPE flight trajectory at 80 km

Species	Grid points	Iteration	CPU time (sec)
	15×51	1040	11.9
5	15×101	1185	26.4
	15×201	1204	53.3
	15×51	1106	19.8
7	15×101	1254	45.2
	15×201	1078	77.6
	15×51	1636	73.1
11	15×101	1463	131.4
	15×201	1680	302.0

0.1 mm in depth from the body surface.

6.8   CPU requirements

The total iteration numbers and CPU times required to obtain the converged solutions are tabulated in Table 6.14. These data were obtained using the free stream condition of the H-II Orbiting Plane (HOPE) flight trajectory at 80 km ($\rho_\infty = 2 \times 10^{-5}$ kg/m^3, $T_\infty = 181$ K, and $M = 25$). All computations were made on a personal computer with 700 MHz CPU. It is confirmed that total iteration number is nearly constant at each number of chemical species. It should also be emphasized that the total CPU times increases only linearly with increasing the normal grid points. This is, as already discussed, one favorable property of the VSL methods. For a NS solver employing a shock-capturing scheme, as the number of grid points increases (i.e. minimum grid spacing decreases), the total computational time increases significantly due to the limitation of the CFL condition.

7   An approach to quick estimation of the stagnation streamline properties

7.1   Motivation

As confirmed from the previous section, the present VSL code can compute hypersonic nonequiliburium flows sufficiently accurately with much shorter computational time than Navier-Stokes solvers. However, sometimes there is an occasion where we are only interested in the stagnation properties of blunted body flows. In this case it would be much better if we could find a more rapid way to compute only the stagnation streamline. In this section, an attempt has been made to compute only the stagnation streamline under the present VSL algorithm.

7.2   Basic idea

As already discussed in the preceding section, the continuity equation and $s-$momentum equation become indeterminate at the stagnation point and hence a special treatment is required. In the $s-$momentum equation, we have a term expressed as

$$A_3 = -\frac{y_{sh}}{\epsilon^2 u_{sh}(1 + \kappa y_{sh}\eta)\mu} \left[y_{sh}\frac{\partial p}{\partial \xi} - \eta \frac{\partial y_{sh}}{\partial \xi} \cdot \frac{\partial p}{\partial \eta} \right] \tag{7.1}$$

This is an indeterminate term at $\xi = 0$ since both u_{sh} and $\partial/\partial\xi$ becomes zero at the stagnation point. To alleviate this inconvenience, we reexpress these terms as an perturbation form and take a limit as $\xi \to 0$.

$$u_{sh} \to \xi u'_{sh}, \quad p' \to \xi p'', \quad y'_{sh} \to \xi y''_{sh} \tag{7.2}$$

Then Eq. (7.1) becomes

$$A_3 = -\frac{y_{sh}}{\epsilon^2 u'_{sh}(1 + \kappa y_{sh}\eta)\mu}\left[y_{sh}\frac{\partial^2 p}{\partial\xi^2} - \eta\frac{\partial^2 y_{sh}}{\partial\xi^2} \cdot \frac{\partial p}{\partial\eta}\right] \tag{7.3}$$

Since u'_{sh}, p'', and y''_{sh} are not zero at the stagnation point, we can estimate these terms and find a solution at the stagnation region. The problem is that these streamwise derivatives cannot be determined only from the stagnation point. They are quantities that depend upon the flow downstream. In the conventional VSL algorithm discussed before, these quantities are evaluated from the shock shape obtained from the previous global iteration and the global iteration is repeated until the difference of the newly obtained shock shape with that obtained from the previous iteration falls in a tolerable limit. On the contrary, if only we can specify these derivatives in advance, it is possible to obtain stagnation properties by only solving along the stagnation streamline. In this case, the total CPU time is expected to be much shorter than for solving the whole flow field using the conventional VSL solution procedure.

As already discussed, the shock shape is expressed using a polynomial form as

$$y_{sh} = y_{sh0} + \frac{1}{2}y_{sh2}\xi^2 + \frac{1}{4}y_{sh4}\xi^4 + \frac{1}{6}y_{sh6}\xi^6 \tag{7.4}$$

Thus the second derivatives of y_{sh} at $\xi = 0$ is

$$\left(\frac{\partial^2 y_{sh}}{\partial\xi^2}\right)_{\xi=0} = y_{sh2} \tag{7.5}$$

It should be noted that u'_{sh} can be evaluated once the shock shape is specified. Hence the downstream properties required before the computation are the second derivatives of shock-layer thickness and pressure at $\xi = 0$, namely

$$y_{sh2} = \left(\frac{\partial^2 y_{sh}}{\partial\xi^2}\right)_{\xi=0}, \quad p_2 = \left(\frac{\partial^2 p}{\partial\xi^2}\right)_{\xi=0} \tag{7.6}$$

It should be noted that y_{sh2} is a single property concerning the shock shape whereas p_2 is a profile along the stagnation streamline. Then the stagnation solution can be obtained if we can specify the values of y_{sh2} and p_2 in advance.

In the present study, we take an approach that the stagnation profile is obtained by solving the flow field not only for the stagnation streamline but also for another streamline adjacent to the stagnation point with specifying only y_{sh2}. In this case, p_2 is obtained as a part of the solution by evaluating numerically using a formula as already shown in Eq. (4.57)

$$p_2 = \left(\frac{\partial^2 p}{\partial\xi^2}\right)_{\xi=0} = 2\frac{p_2 - p_1}{\Delta\xi_1^2} \tag{7.7}$$

where the subscripts $m = 1$ and 2 denote the stagnation point and the adjacent point, respectively.

On the other hand, the first-order streamwise pressure derivative at the adjacent point ($m = 2$) can be evaluated by the three-point backward difference and considering the symmetry condition ($p_0 = p_2$) as

$$\left(\frac{\partial p}{\partial\xi}\right)_2 = \frac{p_2 - p_1}{2\Delta\xi} \tag{7.8}$$

Also if the adjacent streamline is sufficiently close to the stagnation point, the higher-order terms of y_{sh} in Eq. (4.55) can be neglected and the shock shape is expressed approximately as

$$y_{sh} \approx y_{sh0} + \frac{1}{2}y_{sh2}\xi^2 \tag{7.9}$$

Once the shock shape is specified, we can compute the shock properties and the shock derivatives at $m = 1$ and 2. The overall solution procedure of this approach is illustrated in Fig. 7.1. It should be kept in mind that even in the case where we solve the whole flow field, the streamwise derivatives at $m = 2$ are evaluated using Eq. (7.8). Thus the uncertainty concerning the present approach is attributed only to the approximation error of the shock shape given in Eq. (7.9). Thus the solution procedure is almost identical to solving the whole flow field if the specified y_{sh2} is sufficiently accurate.

Next we consider the accuracy of the present approach. Figure 7.2 shows the variation of the stagnation heat flux as a function of y_{sh2}. This figure was obtained by the following procedure: firstly, the whole flow field was solved and the "exact" value of y_{sh2} was evaluated using the least squares curve fitting for the shock standoff distance. Then the stagnation point analysis was performed by shifting y_{sh2} from the "exact" value. As clearly confirmed from this figure, the stagnation heat flux value is insensitive to the change in y_{sh2}. The -100% uncertainty of y_{sh2} means that we totally neglect the terms associated with y_{sh2}. Even in this case, the deviation in the stagnation heat flux from the "exact" value is only 6%. This is expected because, from Eq. (7.9), it is apparent that $y_{sh2} = 0$ corresponds to assuming the shock shape to be parallel to the wall surface. This is still a reasonable assumption if the adjacent streamline is sufficiently close to the stagnation streamline. From Fig. 7.2, it is confirmed that if the uncertainty of y_{sh2} is in the range of 17–18%, we can calculate the stagnation heat flux within 1% of accuracy. Then if we can specify the value of y_{sh2} even to a moderate accuracy, the stagnation properties can be evaluated within a tolerable accuracy.

7.3   Benchmark tests for HEG conditions

The accuracy of the present approach is assessed by using the standard operating condition of the HEG already presented in the subsequent section. First, the whole flow field is solved for every conditions and the values of y_{sh2} were gathered. The result is summarized in Table 7.1. As expected, y_{sh2} is essentially independent of wall catalysis or number of chemical species. It is also recognized that y_{sh2} is slightly enthalpy-dependent. Thus it is reasonable to correlate y_{sh2} with respect to the stagnation enthalpy. From these cataloged data, we obtain a correlation formula of

$$y_{sh2} = 0.172 - 0.00343h_t \tag{7.10}$$

where h_t is the free stream total enthalpy in MJ/kg. With this formula, the present method has been applied to the flow field of the HEG and the results are summarized in Table 7.2 for the 7 species case. For every case, the present stagnation point analysis shows excellent agreement with the original solution procedure solving the whole flow field, although the total iteration number is less than one tenth of the original procedure.

In the present analysis, by solving the adjacent streamline together with the stagnation streamline, the second derivative of the pressure p_2 is obtained as a part of the solution. On the other hand, it is also possible to obtain a solution by correlating and specifying p_2 as well. In this case, it is not necessary to solve an adjacent streamline and then the total iteration number is expected to be much smaller compared to the present approach. Unfortunately, the profile of p_2 has been found to be much sensitive to the change of enthalpy and, if the p_2 is correlated with respect to enthalpy, more than 3% of discrepancy was confirmed for the stagnation heat flux value. Since the source of error is only attributed to the specification of y_{sh2}, the present approach of solving two streamline seems to be a more reasonable choice when considering the trade-off between the computational speed and accuracy.
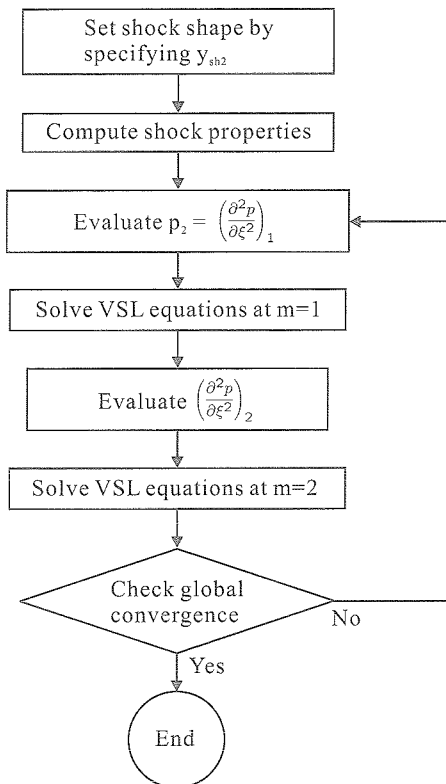
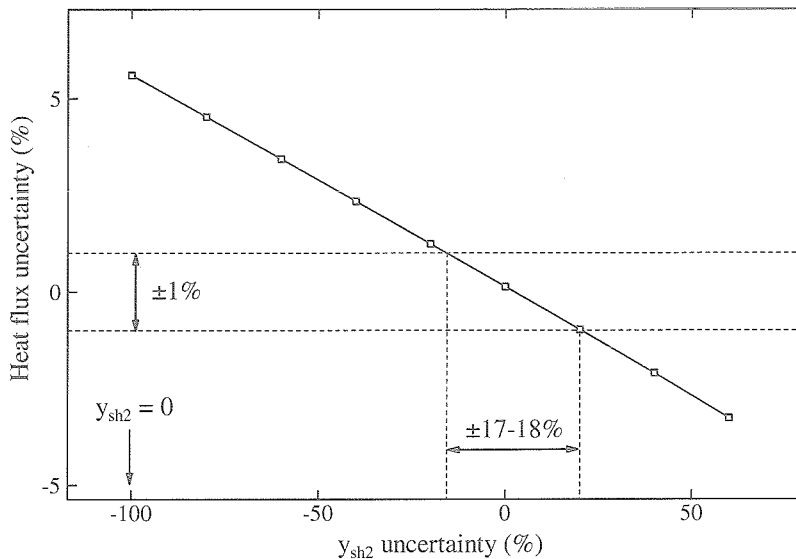Figure 7.1: Solution procedure for solving flow field along the stagnation streamline

Figure 7.2: Variation of the stagnation heat flux as a function of the second derivative of the shock standoff distance, y_{sh2}

Table 7.1: List of y_{sh2} obtained from the VSL solutions under the standard HEG conditions

Cond.	Wall catalysis	Species	y_{sh2}^*
I	NCW	5	0.116
		7	0.117
		11	0.117
	FCW	5	0.114
		7	0.116
		11	0.116
II	NCW	5	0.104
		7	0.106
		11	0.106
	FCW	5	0.104
		7	0.106
		11	0.107
III	NCW	5	0.134
		7	0.134
		11	0.133
	FCW	5	0.132
		7	0.132
		11	0.132
IV	NCW	5	0.121
		7	0.121
		11	0.121
	FCW	5	0.121
		7	0.121
		11	0.121

* Nondimensional value

Table 7.2: Comparison of the stagnation heat flux and the shock standoff distance (7-species model)

Cond.	Catalysis	q_{stg} (MW/m^2)			$y_{sh}/R_n (\times 10^{-2})$			Iteration	
		Case A	Case B	B − A (%)	Case A	Case B	B − A (%)	Case A	Case B
I	NCW	13.7	13.7	0.25	8.03	8.00	−0.37	2000	143
	FCW	16.2	16.2	0.15	7.93	7.91	−0.20	1565	149
II	NCW	24.5	24.5	0.07	7.22	7.21	−0.15	2054	192
	FCW	27.7	27.7	0.11	7.20	7.19	−0.16	1918	160
III	NCW	8.61	8.63	0.16	8.85	8.83	−0.27	2133	171
	FCW	12.0	12.0	0.08	8.73	8.72	−0.13	1867	163
IV	NCW	16.9	16.9	0.04	7.92	7.92	−0.07	2531	199
	FCW	21.4	21.4	0.03	7.85	7.85	−0.02	2414	186

Case A: solve whole flow field
Case B: present stagnation analysis

8   Numerical evaluation of free stream properties for high-enthalpy test facilities using the VSL technique

8.1   Motivation

In an attempt to evaluate the aerothermal characteristics of a hypersonic reentry vehicle by wind tunnel tests, it is of particular importance to estimate the free stream flow properties correctly. For a conventional blow-down type wind tunnel whose flow enthalpy is relatively low, this is not a problem since the reservoir temperature and pressure of such facilities can be measured easily and the flow properties inside the nozzle are described well by the assumption of isentropic expansion [38]. For an impulse test facility including the shock tunnel, on the other hand, the determination of the free stream conditions intrinsically involves considerable difficulties. It is possible to use a nozzle flow calculation code by assuming the reservoir conditions with the measured initial shock speed and the pressure behind the reflected shock as input parameters. However, using this approach, we tend to predict the total enthalpy inside the reservoir much

higher than the actual value since a series of irreversible processes such as the heat loss at the shock tube end wall is not taken into account. For a large scale shock tunnel, the reservoir pressure is of the order of 10 MPa and hence we must take into account the effect of intermolecular forces, i.e. the Van der Waals equation should be used instead of the perfect gas equation of state. Furthermore, as the enthalpy increases, dissociation, recombination, vibrational excitation, and other high-temperature effects become significant and these phenomena involve too many unknowns to model.

For hypersonic and/or high-enthalpy facilities, one traditional approach accepted widely is to deduce the free stream conditions through the use of theoretical formula with measured physical properties at the test section. For example, Fay and Riddell derived an expression of the stagnation heat flux on a sphere for dissociated gases as [39]

$$q_{\mathrm{w}} = 0.76 Pr^{-0.6} (\rho_e \mu_\mathrm{e})^{0.4} (\rho_\mathrm{w} \mu_\mathrm{w})^{0.1}$$
$$\times \sqrt{\left(\frac{du_\mathrm{e}}{dx}\right)_s} (h_\mathrm{e} - h_\mathrm{w}) \left[1 + (Le^{0.52} - 1)\frac{h_D}{h_\mathrm{e}}\right] \tag{8.1}$$

where $h_D = \sum_i C_i \Delta h_i^0$ and the subscript e denote the conditions at the edge of the boundary layer. $(du_\mathrm{e}/dx)_s$ is the tangential velocity gradient at the stagnation point and can be evaluated approximately assuming Newtonian flow. Using measured Pitot pressure and heat flux for the flow field around a sphere, the free stream total enthalpy can be deduced by solving the above equation for h_e. However, this approach may include some error sources due to the following:

1. The derivation of Eq. (8.1) assumes that the flow at the boundary-layer edge is inviscid and in equilibrium.

2. The shock layer thickness should be thin enough for the Newtonian approximation to be valid.

3. The validity of Eq. (8.1) has not been confirmed well for various Prandtl numbers since the original Fay-Riddell formulation has been based on computations for a Prandtl number of 0.76 [40].

4. It is required to introduce some assumptions to deduce flow properties at the boundary edge such as $p_\mathrm{e} = p_t$ or $T_\mathrm{e} = T_t$.

5. If the free stream is dissociated or ionized and in thermochemical nonequilibrium, there is no way to account for such effects.

In fact, the presence of dissociated species in the free stream may be critical for certain wind tunnels, and the flow Mach number and Reynolds number in an arcjet wind tunnel is usually too low for the flow to be hypersonic and inviscid [8]. In these cases, therefore, versatility of the use of Eq. (8.1) may become a problem. In a case where the assumptions introduced in the analytic or empirical approach are violated, it is possible to apply the CFD technique instead of theoretical expressions such as Eq. (8.1) to eliminate these difficulties and this is the main motivation of the present study. The idea is illustrated conceptually in Fig. 8.1. The objective is to obtain the free stream conditions, which are given commonly as input parameters, from the measured properties such as heat flux or Pitot pressure, which are obtained commonly as outputs. This can be regarded as an inverse problem of CFD and clearly different from the traditional role of CFD where the experimentally obtained flow field is numerically reproduced by specifying the free stream conditions as input parameters.

By using CFD, we can readily incorporate the effects of

⊚ thermochemical nonequilibrium state in the shock layer,

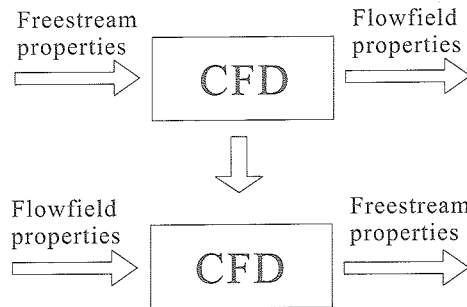⊚ shock-slip,

⊚ finite rate catalysis, and

Figure 8.1: Determination of free stream properties: an inverse problem of CFD.

⊙ free stream dissociation.

In the remainder of the present section, an algorithm is developed to estimate the free stream conditions using the present VSL algorithm. The method is then applied to the HEG standard operational conditions described so far and the accuracy of the present method is investigated.

8.2   Numerical procedure

Typically, we solve a flow field using the CFD solver by specifying free stream properties as boundary condition, and obtain a flow field property such as the stagnation heat flux and pressure. Hence, we can consider that the stagnation heat flux/pressure is estimated through the nonlinear operator F (CFD operation) as a function of the free stream properties. That is,

$$q_{\mathrm{w}} = F_1(p_\infty, T_\infty, M_\infty, \dots) \tag{8.2}$$

$$p_t = F_2(p_\infty, T_\infty, M_\infty, \dots) \tag{8.3}$$

In turn, we now want to obtain free stream properties from the measured aerothermodynamic properties. Since F is a nonlinear multivariable operator, for example, obtaining free stream properties for a set of $(p_t, q_{\mathrm{w}}, \dots)$ corresponds to searching the free stream values which satisfy $F_1 - q_{\mathrm{w}} = 0$ and $F_2 - p_t = 0$. This means that conventional CFD procedures (solve flow field for a set of input parameters) must be performed iteratively as element of an overall iteration algorithm. Hence the total operational cost may be extremely expensive and may not be suitable for practical use if one employs a Navier-Stokes code to evaluate the stagnation properties. In this case, we are only interested in the stagnation point heat flux and pressure and the information concerning whole flow field is not necessary. Therefore, in the present approach, the stagnation point analysis algorithm developed in the preceding section is employed.

8.3   Choice of input parameters

Generally, it is required to specify three independent parameters to completely describe a flow field. Of the three, the Pitot pressure and the stagnation heat flux can be measured directly for any wind tunnel facilities, but the choice of the last variable is a problem. Although it is possible to measure the static pressure at the nozzle exit, the pressure so measured will be different from that of the test section if the model is not located near the exit. However, if one examines the stagnation heat flux distribution for a range of the Pitot pressure, total enthalpy, and free stream Mach number as depicted in Fig. 8.2, it is obvious that the heat flux value is very insensitive to the change of Mach number. Therefore, it is expected that even a nominal value of Mach number gives sufficiently accurate results. In what follows, it is shown that the effect of this approximation on the accuracy of the total enthalpy evaluation is negligible. It is also to be noted that the heat flux changes monotonically with respect to the changes of these three variables, and hence the total temperature can be determined uniquely for a given set of q_{w}, p_t, and M_∞.
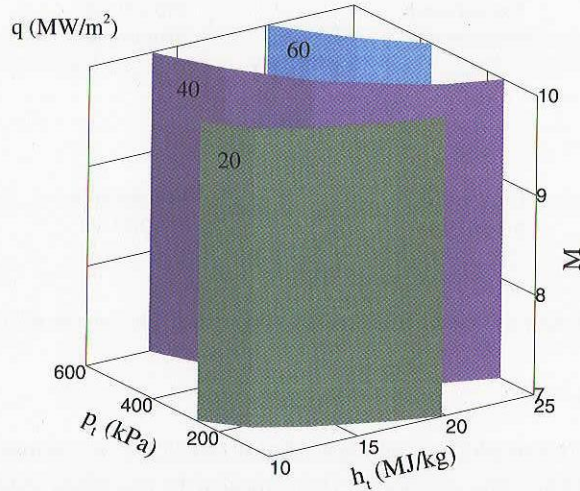
Figure 8.2: Heat flux iso-surface plots under the HEG conditions.

8.4　Algorithm

We need to find a set of (T_∞, p_∞) so that the stagnation heat flux and pressure are equal to the specified values. Here we define the vector $\boldsymbol{G}$ whose components are defined as

$$\boldsymbol{G} = (G_1, G_2)^t = (q_w - q_{w0}, p_w - p_{w0})^t \tag{8.4}$$

where q_w and q_{w0} denote the heat flux value obtained from the CFD analysis and experiment, respectively. Then we try to find T_∞ and p_∞ which satisfy $\boldsymbol{G} = 0$. This falls into the two-dimensional nonlinear root finding problem. One method commonly used is the Newtonian searching algorithm.

$$\Delta \boldsymbol{q} = -A^{-1} \cdot \boldsymbol{G} \tag{8.5}$$

where $\boldsymbol{q} = (T_\infty, p_\infty)^t$ and A is the Jacobian matrix defined as $A = \partial \boldsymbol{G}/\partial \boldsymbol{q}$. Needless to say, we can not obtain the analytical expression of A, so that A must be evaluated in a numerical way. In the present algorithm, the approximate Newtonian method of Broyden [42] was employed. In this method, the Jacobian matrix at iteration number k, A^k, is evaluated approximately from the previous values at $k - 1$ as

$$A^k = A^{k-1} + \frac{(\Delta \boldsymbol{G}^{k-1} - A^{k-1} \cdot \Delta \boldsymbol{q}^{k-1}) \otimes \Delta \boldsymbol{q}^{k-1}}{\Delta \boldsymbol{q}^{k-1} \cdot \Delta \boldsymbol{q}^{k-1}} \tag{8.6}$$

This formula is based on the idea of getting A^k by making the least change to A^{k-1} consistent with the secant equation of the form

$$A^k \cdot \Delta \boldsymbol{q}^{k-1} = \Delta \boldsymbol{G}^{k-1} \tag{8.7}$$

The initial Jacobian matrix A^0 is numerically evaluated by computing $\boldsymbol{G}$ at the initial set of T_∞ and p_∞, and further increasing these values to a certain extent.

The overall solution procedure is illustrated in Fig. 8.3. It is emphasized that the stagnation analysis method developed in the preceding section is employed here since properties of interest are only the stagnation heat flux and pressure.

8.5　Benchmark test for the HEG operating conditions

The present algorithm was applied to the four HEG standard operating conditions presented in the preceding section. The stagnation point heat flux and pressure in Table 6.10 were used as a set of specified quantities and the free stream enthalpy was computed by varying the Mach number from 5 to 10. For
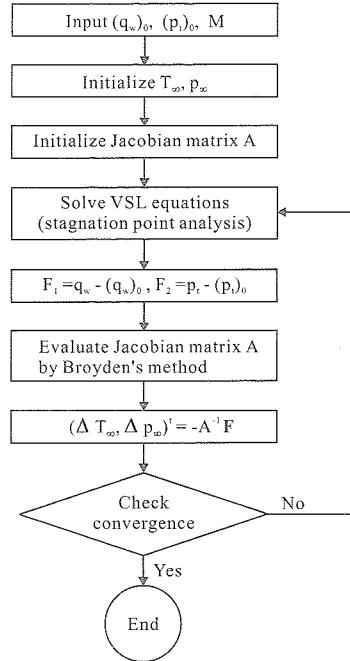
Figure 8.3: Algorithm flowchart

comparison, the enthalpy was also evaluated by applying Eq. (6.1). The comparison of the estimated free stream enthalpy is compared with the original value in Table 8.1. Using Broyden's method, in every case, a converged solution can be obtained within 7–8 iterations at most. As expected, the estimated total enthalpy agrees very well with the specified value irrespective of the Mach number assumption. This indicates that the free stream total enthalpy can be evaluated sufficiently accurately by the present approach even with an approximate free stream Mach number. On the other hand, more than 4 % of prediction error can be observed if the correlation formula of Eq. (6.1) is employed instead of the present VSL algorithm.

Table 8.1: Comparison of specified/estimated free stream total enthalpy

Cond.	h_t(specified) MJ/kg	$M = 5$		$M = 7.5$		$M = 10$		Eq. 6.1	
		h_t	Δh_t (%)	h_t	Δh_t (%)	h_t	Δh_t (%)	h_t	Δh_t (%)
I	16.54	16.48	−0.40	16.55	0.02	16.53	−0.06	16.71	1.00
II	19.18	19.12	−0.31	19.20	0.11	19.20	0.09	18.41	−4.03
III	11.35	11.27	−0.68	11.34	−0.08	11.33	−0.18	11.23	−1.02
IV	14.36	14.26	−0.69	14.35	−0.02	14.35	−0.03	13.74	−4.27

8.6   Accuracy estimation

Next, the accuracy of the present approach is examined as follows. Noting that $h_t = h_t(p_t, M_\infty, q_w)$, and using the Taylor expansion, we obtain

$$\frac{\Delta h_t}{h_t} = \theta_{p_t} \frac{\Delta p_t}{p_t} + \theta_{q_w} \frac{\Delta q_w}{q_w} + \theta_{M_\infty} \frac{\Delta M_\infty}{M_\infty} \tag{8.8}$$

where the sensitivity coefficients θ_{p_t}, θ_{q_w}, and θ_{M_∞} can be defined as

$$\theta_{p_t} = \frac{p_t}{h_t} \cdot \frac{\partial h_t}{\partial p_t}, \quad \theta_{q_w} = \frac{q_w}{h_t} \cdot \frac{\partial h_t}{\partial q_w}, \quad \theta_{M_\infty} = \frac{M_\infty}{h_t} \cdot \frac{\partial h_t}{\partial M_\infty} \tag{8.9}$$

We try to estimate θ_{q_w} and θ_{p_t} in the conditions of interest (θ_{M_∞} is omitted here since it is negligibly small). Since we cannot obtain these coefficients analytically, the partial differences $\partial h_t/\partial p_t$ and $\partial h_t/\partial q_w$ are estimated approximately in a finite difference fashion with computing h_t for various p_t, and q_w. Figure 8.4
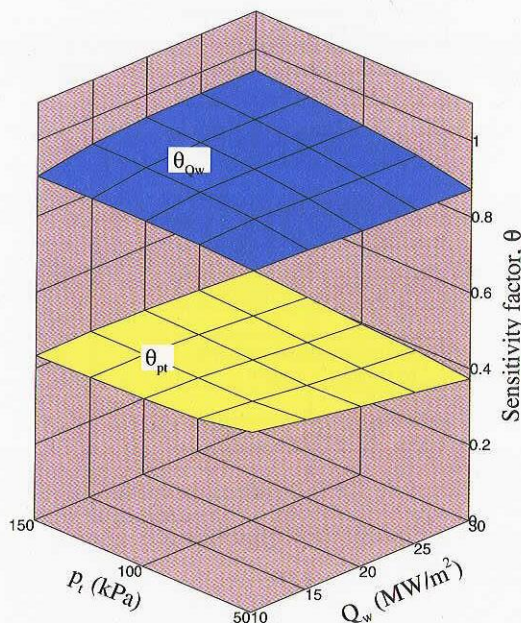
Figure 8.4: Distribution of sensitivity coefficients.

depicts the distribution of these sensitivity coefficients as a function of q_w and p_t. It is observed that both of the sensitivity coefficients indicates less than unity for every conditions of interest. Thus, using the present approach, it is at least expected that the predicted h_t does not amplify the uncertainties associated with the measurement errors of q_w and p_t.

8.7   On the credibility of the present algorithm

The accuracy of the present algorithm can be enhanced as we improve the accuracy of measured flow properties. This can be achieved by the improvement of measuring techniques, application of the redundant measurement techniques, developing an uncertainty analysis procedure, etc. However, first, it is obvious that the accuracy of the VSL algorithm itself must be sufficiently guaranteed. This is directly connected with the issue of CFD Verification and Validation (V & V) process [43]. We comment on this regarding the present VSL technique below.

By definition, verification is a process of assessing the credibility of the numerical algorithm to solve a specific set of governing equations and boundary conditions [44]. It may contain the assessment of the sensitivity of results to grid distribution, particularly for complex geometries, and to numerical viscosity added to capture strong discontinuities such as shock waves or contact surfaces. As far as the present method is concerned, however, it should be noted that the flow field we want to solve is restricted to very simple cases, i.e. hypersonic flow around a sphere, so that sensitivity testing with respect to the grid deformation is not required. Also, since the VSL algorithm is a shock-fitting scheme, no numerical dissipation term is introduced and thus the algorithm is free from numerical errors associated with this. Therefore, the only process needed to verify the present code is grid convergence testing. The Grid Convergence Index (GCI) [43], may be available to estimate the discretization error.

Validation, in turn, is a process to assess whether the governing equations or the physical model employed is accurate enough to reproduce the actual physics in a range of conditions of interest. Regarding the present method, this includes the assessment of 1) whether the VSL equations are reasonable representations of the Navier-Stokes equations, 2) transport properties for multicomponent gas mixtures, and 3) chemical reaction rates for nonequilibrium flow fields. As noted earlier, the VSL equations are a subset of the Navier-Stokes equations by keeping terms up to second order with respect to $\epsilon \equiv 1/\sqrt{Re}$. Concerning

the first issue, as can be confirmed from the previous section, the present VSL code is found to be a good representation of the NS solver for most conditions of interest. The choice of physical models associated with transport properties and chemical reaction speed may also have an impact on the accuracy of the result obtained. It is possible to investigate the sensitivity of the solution to the change of these models by comparing the result of one model with that of others. Empirically, however, it is expected that the effect of the choice of chemical models on the predicted value of heat flux is relatively minor. Also the stagnation pressure is less sensitive to the chemical state since the pressure distribution is essentially determined by the balance of momentum and is not so much affected by the chemical reactions.

9   Summary

A new viscous shock-layer code has been developed. By using the present code, the hypersonic flow around a hemisphere which may be in chemical nonequilibrim can be solved typically within 1 minute using a conventional personal computer.

The accuracy of the code was examined by comparing with Navier-Stokes results and essentially identical results have been obtained for a perfect gas case. The VSL results were further compared with the Navier-Stokes computations for the stagnation heat flux/pressure for a wide range of Mach numbers and Reynolds numbers. It has been confirmed that the difference in the stagnation heat flux is around 1 % at most for a Reynolds number range from 10^3 to 10^5. Thus the present VSL code was found to be sufficiently accurate compared to conventional Navier-Stokes solvers for most practical problems of interest. The code is further validated by comparing with other VSL/Navier-Stokes results under the flight conditions of OREX/AFE and reasonable agreement has been confirmed.

Next an efficient technique has been proposed to obtain stagnation properties of blunt body problems by only solving two streamlines in the stagnation region. In this method, by only specifying the streamwise second derivative of the shock standoff distance, stagnation properties can be obtained with less than one tenth of the CPU time compared to solving the whole flow field by the original VSL solution procedure. The second derivative of the shock standoff distance was correlated with the free stream enthalpy concerning the four standard conditions of HEG, and the stagnation point heat flux obtained from the present approach has been confirmed to be essentially identical to the value obtained by solving the whole flow field.

Also an algorithm has been developed to deduce free stream total enthalpy of high enthalpy shock tunnels. In this algorithm, free stream properties can be iteratively computed by specifying measured stagnation heat flux and Pitot pressure plus nominal Mach number. The method was applied to the HEG conditions and it has been found that the accuracy of the present approach is sufficient.

References

[1] Davis, R. T., "Numerical Solution of the Hypersonic Viscous Shock-Layer Equations," *AIAA Journal*, Vol. 8, No. 5, May 1970, pp. 843–851.

[2] Anderson, E. C. and Moss, J. N., "Numerical Solution of The Hypersonic Viscous-Shock-Layer Equations for Laminar, Transitional, and Turbulent Flows of a Perfect Gas over Blunt Bodies," NASA TN D-7865, Feb. 1975.

[3] Miner, E. W. and Lewis, C. H., "Hypersonic Ionizing Air Viscous Shock-Layer Flows over Nonanalytic Blunt Bodies," NASA CR-2550, May 1975.

[4] Shinn, J. L. and Simmonds, A. L., "Comparison of Viscous Shock-Layer Heating Analysis with Shuttle Flight Data in Slip Flow Regime," *Thermal Design of Aeroassisted Orbital Transfer Vehicles*, Vol. 96, Progress in Astronautics and Aeronautics, (Nelson, H. F. ed., AIAA, New York), 1985, pp. 491–510.

[5] Lee, J.-H., "Basic Governing Equations for the Flight Regimes of Aeroassisted Orbital Transfer Vehicles," *Thermal Design of Aeroassisted Orbital Transfer Vehicles*, Vol. 96, Progress in Astronautics and Aeronautics, (Nelson, H. F. ed., AIAA, New York), 1985, pp. 3–53.

[6] Weber, Y. and Anderson Jr., J., "Comparison of Chemical Kinetic Rate Mechanisms for High-Temperature Air, Including Electronic Energy," *AIAA J.* Vol. 30, No. 12, 1992, pp. 2980–2982.

[7] Kolodziej, P. and Stewart, D. A., "Nitrogen Recombination on High-Temperature Reusable Surface Insulation and the Analysis of its Effect on Surface Catalysis," AIAA Paper AIAA-87-1637, June 1987.

[8] Park, C., "Assessment of Two-Temperature Kinetic Model for Ionizing Air," *J. Thermophys. Heat Trans.*, Vol. 3, No. 3, July 1989, pp. 233–244.

[9] Park, C., *Nonequilibrium Hypersonic Aerothermodynamics*, Wiley, New York, 1990, pp. 35–38.

[10] Gupta, R. N., Yos, J. M., Thompson, R. A., and Lee, K.-P., "A Review of Reaction Rates and Thermodynamic and Transport Properties for an 11-Species Air Model for Chemical and Thermal Nonequilibrium Calculations to 30000K," NASA RP 1232, Aug. 1990.

[11] Park, C., Howe, J. T., Jaffe, R. L., and Candler, G. V., "Chemical-Kinetic Problems of Future NASA Missions," AIAA Paper AIAA 91-0464, Jan. 1991.

[12] Yos, J. M., "Transport Properties of Nitrogen, Hydrogen, Oxygen, and Air to 30,000 K," Technical Memorandum RAD TM-63-7, AVCO-RAD, Wilmington, Mass., Mar. 1963.

[13] Curtiss, C. F. and Hirschfelder, J. O., "Transport Properties of Multicomponent Gas Mixture," *J. Chem. Phys.*, Vol. 17, No. 6, June 1949, pp. 550–555.

[14] Waskiewicz, J. D., Murray, A. L. and Lewis, C. H., "Hypersonic Viscous Shock-Layer Flow over a Highly Coolded Sphere," *AIAA J.*, Vol. 16, No. 2, Feb. 1978, pp. 189–192.

[15] Billig, F. S., "Shock-Wave Shapes around Spherical- and Cylindrical-Nosed Bodies," *J. Spacecraft and Rockets*, Vol. 4, No. 6, June 1967, pp. 822–823.

[16] Anderson, Jr., J. D., *Hypersonic and High Temperature Gas Dynamics*, McGraw-Hill, New York, 1989, p. 635.

[17] Gupta, R. N., Lee, K. P., Zoby, E. V., Moss, J. N., and Thompson, R. A., "Hypersonic Viscous Shock-Layer Solutions over Long Slender Bodies –Part I: High Reynolds Number Flows," *J. Spacecraft and Rockets*, Vol. 27, No. 2, March–April 1990, pp. 175–184.

[18] Gupta, R. N., Moss, J. N., and Price, J. M., "Assessment of Thermochemical Nonequilibrium and Slip Effects for Orbital Reentry Experiment (OREX)," AIAA Paper AIAA 96-1859, 1996.

[19] Wada, Y. and Liou, M.-S., "A Flux Splitting Scheme with High-Resolution and Robustness for Discontinuities, " AIAA-94-0083, 1994.

[20] Anderson, W. K., Thomas, J. L. and van Leer, B. "Comparison of Finite Volume Flux Vector Splittings for the Euler Equations, " *AIAA Journal*, 24, 1986, pp. 357–372.

[21] Jameson, A. and Yoon, S., "Lower-Upper Implicit Schemes with Multiple Grids for the Euler Equations," *AIAA J.*, 25, 1987, pp. 929–935.

[22] Lees, L., "Laminar Heat Transfer over Blunt-Nosed Bodies at Hypersonic Flight Speeds," *Jet Propulsion*, Vol. 26, No. 4, 1956, pp. 259-269.

[23] Müller, S., Yamaleev, N., and Klomfass, A., "A Comparative Study of Navier-Stokes and Viscous Shock Layer Solutions for a Wide Range of Reynolds and Mach Numbers," December, 1995 (taken from http://citeseer.ist.psu.edu/cis).

[24] Klomfass, A., and Müller, S., "Calculation of Stagnation Streamline Quantities in Hypersonic Blunt Body Flows," *Shock Waves*, Vol. 7, pp. 13–23, 1997.

[25] Gray, J. D., "Summary Report on Aerodynamic Characteristics of Standard Models HB-1 and HB-2," AEDC-TDR-64-137, July 1964.

[26] Kuchi-Ishi, S., Watanabe, S., Nagai, S., Tsuda, S., Koyama, T., Hirabayashi, N., Sekine, T., and Hozumi, K., "Comparative Force/Heat Flux Measurements between JAXA Hypersonic Test Facilities Using Standard Model HB-2 (Part 1: 1.27 m Hypersonic Wind Tunnel Results)," JAXA Research and Development Report JAXA-RR-04-035E, March 2005.

[27] Boudreau, A. H., "Performance and Operational Characteristics of AEDC/VKF Tunnels A, B, and C," AEDC-TR-80-48, 1981.

[28] Kurotaki, T., "Construction of Cataytic Model on SiO_2-Based Surface and Application to Real Trajectory," AIAA Paper AIAA 2000-2366, 2000.

[29] Gupta, R. N., Jones, J. J., and Rochelle, W. C., "Stagnation-Point Heat-Transfer Rate Predictions at Aeroassist Flight Conditions," NASA TP-3208, Sept. 1992.

[30] Hamilton, H. H., Gupta, R. N., and Jones, J. J., "Flight Stagnation-Point Heating Calculations on Aeroassist Flight Experiment Vehicle," *J. Spacecraft and Rockets*, Vol. 28, No.1, Jan.-Feb. 1991, pp. 125-128.

[31] Verant, J. L., "Numerical Enthalpies Rebuilding for Perfect Gas and Nonequilibrium Flows. Application to High Enthalpy Wind-Tunnels," ONERA Report RT No. 69/6121 SY, HT-TN-E-1-201-ONER, 1995.

[32] Coquel, F., and Marmignon, C., "Roe Type Linearization for the Euler Equations for Weakly Ionized Multicomponents and Multi-Temperature Gas," AIAA Paper AIAA 95-1675, June 1995.

[33] Sagnier, P., Masson, A., Mohamed, A. K., Verant, J. L., and Devezeaux, D., "Synthesis of MSTP calibration campaigns in ONERA F4 hot shot wind tunnel," *Proceedings of the 16th International Congress on Instrumentation in Aerospace Simulation Facilities*, Dayton, OH, 1995.

[34] William, J., Verant, J.-L., and Sagnier, P., "An Efficient Numerical Tool for Blunted Bodies Stagnation Line Rebuilding with Weakly Ionized Thermochemical Nonequilibrium Flows, " Proceedings of 15th IMACS world congress on scientific computation, modeling, and applied mathematics, 1997.

[35] Karl, S., Martinez-Schramm, J., and Hannemann, K., "High Enthalpy Cylinder Flow in HEG: A Basis for CFD Validation," AIAA Paper AIAA 2003-4252, June 2003.

[36] Eitelberg, G., "First Results of Calibration and Use of the HEG," AIAA Paper AIAA 94-2525, 1994.

[37] Hannemann, K., Schnieder, M., Reimann, B., and Martinez-Schramm, J., "The Influence and the Delay of Driver Gas Contamination in HEG," AIAA Paper AIAA 2000-2593, 2000.

[38] Pope, A. and Goin, K. L., *High-Speed Wind Tunnel Testing*, Wiley, New York, 1965.

[39] Fay, J. A. and Riddell, F. R., "Theory of Stagnation Heat Transfer in Dissociated Air," *Journal of Aeronautical Sciences*, Vol. 25, No. 2, Feb. 1958, pp. 73–85.

[40] Walpot, L. M. G., Simeonides, G., Muylaert, J., and Bakker, P. G., "High Enthalpy Nozzle Flow Sensitivity Study and Effects on Heat Transfer," *Shock Waves*, Vol. 6, 1996, pp. 197–204.

[41] Pope, R. B., "Measurements of Enthalpy in Low-Density Arc-Heated Flows," *AIAA Journal*, Vol. 6, No. 1, Jan. 1968, pp. 103–110.

[42] Press, W. H., Teukolsky, S. A., Vetterling, W. T., and Flannery, B. P. *Numerical recipes in C* 2nd ed, Cambridge Univ. Press, Cambridge, 2002 pp. 389–392.

[43] Roache, P. J., *Verification and Validation in Computational Science and Engineering*, Hermosa, New Mexico, 1998.

[44] Rizzi, A. and Vos, J., "Toward Establishing Credibility in Computational Fluid Dynamics Simulations," *AIAA Journal*, Vol. 36, No. 5, May 1998, pp. 668–675

JAXA

Japan Aerospace Exploration Agency